Mid-Holocene climate of the Tibetan Plateau and hydroclimate in three major river basins based on high-resolution regional climate simulations

5 Yiling Huo[1], William Richard Peltier[1], and Deepak Chandan[1]

[1] Department of Physics, University of Toronto, Toronto, M5S 1A7, Canada

Correspondence to: Yiling Huo (yhuo@physics.utoronto.ca)

Abstract. The Tibetan Plateau (TP) ~~exerts strong influence on both regional and global climate through thermal and mechanical forcings. The TP also~~ contains the headwaters of ~~large~~major Asian rivers that sustain billions of people and

10 ~~numerous ecosystems.~~plays an important role in both regional and global climate through thermal and mechanical forcings. Understanding the characteristics and changes to the hydrological regimes on the TP during the mid-Holocene (MH) will help understand the expected future changes. Here, an analysis of the hydroclimates over the headwater regions of three major rivers originating in the TP, namely the Yellow, Yangtze and Brahmaputra rivers is presented, using ~~an ensemble of climate simulations, which have been~~ dynamically downscaled ~~to 10 km resolution with~~climate simulations constructed

15 using the Weather Research and Forecasting Model (WRF) coupled to the hydrological model WRF-Hydro. ~~Basin integrated changes in the seasonal cycle of hydroclimatic variables are considered. In the global model, we have also incorporated~~ Green Sahara (GS) boundary conditions ~~in order to compare with standard MH simulations (which do not include GS) and~~have also been incorporated into the global model so as to capture ~~interactions~~the remote feedbacks between the ~~GS~~Saharan vegetation and the river hydrographs over the TP. Model-data comparisons show that the dynamically

20 downscaled simulations significantly improve the regional climate simulations over the TP in both the modern day and the MH, highlighting the crucial role of downscaling in both present-day and past climates~~, although both global and regional models have a cold bias in modern day simulations and underestimate the wet anomalies inferred from proxy data in the east and southeast part of the TP.~~. TP precipitation is also ~~greatly influenced~~strongly affected by the ~~inclusion~~greening of ~~a GS~~the Sahara, with a particularly large increase ~~predicted~~ over the southern TP, as well as a delay in the monsoon withdrawal. The

25 ~~model performance was~~simulation results were first ~~evaluated~~validated over the upper basins of the three rivers before the hydrological responses to the MH forcing ~~in streamflow as well as temperature, rainfall and snowmelt~~ for the three basins were quantified~~ via~~. Both the upper Yellow and Yangtze rivers exhibit a decline in streamflow during the MH, especially in summer, which is a combined effect of less snowmelt and stronger evapotranspiration. The GS forcing caused a rise in

temperature during the ~~WRF simulations~~MH, as well as larger rainfall but less snowfall and greater evaporative water losses.

30   The Brahmaputra River runoff is simulated to increase in the MH, due to greater net precipitation.

1 Introduction

The Tibetan Plateau (TP~~) and its surrounding regions,~~), often referred to as the Third Pole, with an average elevation exceeding 4000 m and an area of 2.5×10^6 km^2, constitute the ~~most extensive and~~ highest and largest plateau in the world. The TP also has the most extensive cryosphere outside the Arctic/Greenland and the Antarctic regions (Yao et al., 2012),

35   including snow cover, glaciers and permafrost. ~~As a unique geological and geographical unit~~Moreover, the TP ~~exerts a profound influence~~is also widely believed to have a huge impact on ~~both~~ the ~~Asian~~local and global climate through thermal and mechanical ~~and thermal~~ forcing ~~mechanisms~~ (Kutzbach et al., 1993; An et al., 2001; Molnar et al., 2010). Climate over the TP, ~~which is characterized by a wet and~~featuring warm ~~summer~~wet summers and ~~a cool and~~cold dry ~~winter~~winters, is extremely sensitive to global ~~climate change~~warming and has ~~experienced~~undergone rapid and ~~pronounced~~profound changes

40   in recent ~~decades~~years (Lehnert et al., 2016; Yao et al., 2019). With an elevation gradually decreasing from the northwest to the southeast, the TP also acts as the "water tower" and the source region of ~~major Asian~~large rivers in Asia that flow down to almost half of humanity, including the Yellow, Yangtze and Brahmaputra (Yarlung Tsangpo) Rivers (Immerzeel et al., 2020).

The Yellow River, which is often referred to as the cradle of the Chinese civilization, ~~originates~~rises in the northern part of

45   the TP (Fig. 1) and supports ~~30%~~nearly one third of the China's population (Huang et al., 2009). It passes ~~through~~across the Loess Plateau and the North China Plain, before emptying into the ~~Bohai Sea~~ocean on the east coast of China. The Yellow River's headwaters are ~~situated~~located in the Bayan Har Mountains in the northern TP. Its water resources are vital to the unique but fragile ~~and unique temperate, alpine, and wetland~~ecosystems ~~within~~in the upper Yellow River Basin (UYEB) and are extremely sensitive to climate change. The longest river in Asia, the Yangtze, ~~rises~~originates in the Tanggula

50   Mountains over the eastern part of the TP and flows eastwards to the East China Sea (Fig. 1). Its drainage basin comprises one-fifth of China's land area, which is home to nearly a third of the country's population. The Brahmaputra River, which originates in the southern TP and flows eastwards before turning southward into India in Arunachal Pradesh, is an important trans-boundary river. After entering India, it turns southwestward and eventually enters Bangladesh where it merges with the Padama River in the Ganges Delta. ~~Dramatic~~There is dramatic climatic heterogeneity ~~exists~~within its drainage area, from

55   the ~~dry and~~cold dry upper region with an ~~elevation~~altitude higher than 5000 m, which features glaciers and permanent snow, to the humid and hot downstream area that is only 200 m above sea level. The Brahmaputra River flows across four Asian countries including countries with the two largest populations in the world, China and India. Understanding hydrological processes of these rivers is necessary for ~~informed current and future sustainable~~water resource management ~~of their water resources~~and are of significant economic importance for these countries. ~~Thus, it is important to understand how climate~~

60   ~~change will impact streamflow and, hence, available water resources on a basin scale.~~

~~Meteorological observations on~~Observations over the TP ~~indicate~~suggest a ~~surface~~ warming trend that is twice as large as ~~that observed globally~~the global average (IPCC, 2013), ~~accompanied by~~with spatial differences in ~~changes to~~ precipitation and ~~glaciers~~ glacier changes (Yao et al., 2012). An increasing trend in precipitation has been observed to be occurring in the western and central TP and a smaller precipitation increase has been detected in the eastern TP (Zhou et al., 2019). ~~Most regions of the~~The TP ~~have~~has generally become wetter and warmer ~~and wetter, while the southern TP has become warmer and drier,~~ during the past three decades, although the southern part has turned drier (Yang et al., 2014). ~~Glacier melt is~~As an important hydrologic process in ~~cold~~mountain regions, ~~that significantly modifies streamflow~~the melting of glaciers can greatly modify the characteristics, ~~such as quantity~~ of streamflow, including magnitude, timing, and variability ~~of flows over space and time~~ (Kaser et al., 2010; Immerzeel et al., 2020). ~~Changes in~~Both temperature and precipitation ~~are expected to seriously affect the melt characteristics of mountain glaciers~~changes will significantly influence glacier melt (Barnett et al., 2005; Immerzeel et al., 2020), inducing heterogenous responses over different parts of the TP. ~~In a warmer climate,~~Higher temperature can significantly enhance glacier melt ~~will be enhanced due to the disappearance of~~ by removing fresh snow and ~~the associated decrease of the~~ hence decreasing surface albedo (Barnett et al., 2005). Glacier melt ~~especially affects~~ is a particularly important source of streamflow ~~in~~during warm and dry seasons ~~(Kaser et al., 2010) and~~, which will ~~increase~~enhance the ~~water supply to~~ downstream discharge of the rivers (Kaser et al., 2010; Yao et al., 2004). However, this increase is transitory and is expected to cease when the glaciers have largely retreated (Yao and Yao, 2010). ~~Over a long time period,~~The eventual disappearance of mountain glaciers ~~are predicted to disappear, leading to a decline~~after melting for a long time will result in ~~river flow~~a drop in ~~the~~ streamflow in summer ~~season~~ (Immerzeel et al., 2020) and ~~posing serious and unprecedented~~pose severe threat to access to water resources in the TP and downstream ~~regions~~areas (Kehrwald et al., 2008).

Rivers that originate in the TP often suffer from a scarcity of data ~~required~~necessary for hydrological simulation ~~and water resource assessment due to~~because of the extreme conditions under which measurements must be acquired. Regional hydrological ~~modeling~~simulation in these ungauged ~~regions has~~areas therefore ~~attracted increased attention in water resource management research but~~ faces significant technical challenges due to the complex regional topography. The resolution of ~~current~~most global climate models (GCMs) is ~~not sufficient~~insufficient for this ~~area~~region, because regional climate over the TP is strongly affected by the steep topographic gradients that are poorly resolved in global models. This hinders ~~characterizing~~our ability to characterize the water cycle ~~and~~, study regional climate change ~~studies in this area~~impacts and ~~finding~~find solutions to ~~international~~local water ~~resource issues. For this reason,~~ problems. Therefore, this study has dynamically downscaled global climate simulations ~~need to be downscaled~~ to ~~scales at which~~better resolve important regional topographic features ~~are better resolved~~.

The study of past climate conditions is an important tool in any effort to understand the mechanisms influencing present and future climate and its variability. In addition, understanding the range of variability will help to improve climate models that are used to simulate the ~~region's~~regional response to a ~~range~~variety of abrupt and long-term changes in temperature, atmospheric circulation ~~patterns~~, and moisture sources, which in turn regulate the ~~amount of~~ river discharge flowing out of

95　the TP. The mid-Holocene (MH, approximately 6000 years ago) is one of the most widely studied periods of the Quaternary and is a period of focus for the Paleoclimate Modelling Intercomparison Project (PMIP). ~~During~~In the MH, variation in the Earth's orbital ~~configuration~~parameters led to differences in the latitudinal and seasonal distribution of incoming solar radiation (Berger 1978), resulting in a climate that was remarkably different from that of the present day. ~~During summer (winter), the~~The insolation was anomalously strong (weak) in summer (winter) over the Northern Hemisphere (NH~~)~~),

100　leading to an enhancement of the seasonal cycle. A temperature optimum for the TP during the MH has been ~~recorded~~indicated by pollen data (Herzschuh et al., 2006; Lu et al., 2011; Ma et al., 2014). Understanding MH climatic changes over the TP ~~are crucial to understanding~~will help understand the impact of the recent/modern global warming and ~~to predicting~~predict future climate change (Wanner et al., 2008). During the MH, South and East Asian monsoons are expected to have been enhanced due to the increased boreal summer insolation (Huo et al., 2021; Maher, 2008; Herzschuh, 2006~~;~~

105　~~Maher, 2008~~). However, compared with the reconstructions, regional biases and large spreads are found in numerical simulations of the MH climate by the PMIP models, in particular, over and around the TP (Zheng et al., 2013).

During the MH, changes in insolation and albedo feedbacks also strengthened the African monsoon, making northern Africa much wetter than today (Skinner and Poulsen, 2016). Lakes, rivers, and wetlands formed and developed in the now arid regions of northern Africa and led to a northward extension of the vegetation cover over the Sahara, i.e., a "Green Sahara"

110　(GS; ~~Pausata et al., 2020;~~Chandan and Peltier, 2020; Pausata et al., 2020). Studies have shown that ~~the remote feedbacks associated with~~ a vegetated Sahara and the strengthened African monsoon can ~~alter~~enhanced the Asian monsoon by altering the Walker circulation through changes in tropical Atlantic SSTs~~, which in turn enhanced the Asian monsoon~~ (Pausata et al., 2017). The TP, which is situated within the region influenced by the Asian monsoon (Conroy and Overpeck, 2011) is thus also affected by the greening of the Sahara. One of the key goals of the present study is to outline the remote response of the

115　MH TP climate to the GS teleconnection by analysing a set of simulations in which the land cover is changed from desert to shrubland over a large part of northern Africa (Chandan and Peltier, 2020~~) and~~.). Since there are few studies ~~have investigated~~that characterize the runoff ~~characteristics~~ over the TP under the MH climate conditions, in this study we also analyse the hydrological response of the TP rivers to the MH climate forcing.

The objective of this article is thus to first evaluate the performance of the coupled UofT-CCSM4-WRF-Hydro model over

120　the TP and then analyse the response of hydroclimate over the three rivers over the TP to MH orbital forcing and remote GS feedback, ~~based on~~using high-resolution~~, dynamically downscaled~~ regional climate simulations. ~~Details concerning the~~Section 2 describes experimental design and the model configurations ~~used in the downscaled simulations are given in the next section (Sect. 2).~~. The validation of the results is discussed in Sect. 3, before the general patterns of MH anomalies are outlined. The central point of this study is hydroclimatological anomalies in the upper Yellow, Yangtze and Brahmaputra

125　River basins (UYEB, UYAB and UBB, respectively), which is presented in Sect. 4. Section 5 summarizes the main results of the present study.

2 Model descriptions and experimental design

2.1 Experimental design

This study employs dynamical downscaling, a modelling methodology based upon the use of a dynamically consistent, physically based high-resolution regional climate model (RCM) to downscale global climate simulations so as to better account for regional climate feedbacks ~~in the climate system~~. The global climate simulations used to drive the RCM have been obtained using the University of Toronto version of the National Center for Atmospheric Research (NCAR) Community Climate System Model version 4 (UofT-CCSM4; Peltier and Vettoretti, 2014; Chandan and Peltier, ~~2017,~~ 2018). The global climate simulations are then dynamically downscaled to 10-km resolution using the Weather Research and Forecasting (WRF) model version 4.1 with four different convection parameterization schemes, constituting a small physics ensemble. We have also coupled WRF-Hydro (Gochis et al., ~~2018~~2020) to the WRF model as a hydrological extension package for hydrometeorological (e.g., rainfall, runoff, groundwater flow, streamflow) simulations, which will also be a ~~central point~~primary focus of the analyses to be discussed herein. The ~~fully~~synchronously coupled coupled WRF-Hydro modelling system outperforms the WRF-only model and thus has been employed in atmosphere-hydrology simulations over various domains around the globe (Senatore et al., 2015; Kerandi et al., 2017; Somos-Valenzuela and Palmer, 2018). ~~We focus our~~Our hydroclimatic analysis is focused on the upper Yellow, Yangtze and Brahmaputra River basins (UYEB, UYAB and ~~YBB~~UBB, respectively), the headwaters of which are all located on the TP.

Four global climate simulations were performed using UofT-CCSM4 at approximately 1° resolution, one for the historical period (1980-94), one for the preindustrial (PI) reference period and two for the MH. UofT-CCSM4 is based on the standard CCSM4 (Gent et al., 2011), but specific modifications have been made to the diapycnal diffusivity of the ocean component to make it more appropriate for paleoclimate simulations (Peltier and Vettoretti, 2014; Chandan and Peltier, 2017). ~~The same PI and MH global simulations have also been employed in Huo et al. (2021)~~These changes have been taken into account in both the MH and PI simulations to avoid introducing ambiguity related to different diapycnal mixing schemes when these two simulations are compared. Huo et al. (2021) has employed the same PI and MH global simulations for the purpose of studying MH monsoons in South and Southeast Asia. The two MH simulations differ from each other in ~~terms of the prescribed~~their land surface ~~modifications~~boundary conditions over northern Africa (Chandan and Peltier, 2020) but otherwise share the same orbital parameters and trace gases as the PMIP4 recommendations (Otto-Bliesner et al., 2017): MH_{REF} is the "control MH" which uses the same land surface as in PI, while MH_{GS} extends MH_{REF} by adding the GS vegetation. Compared to the PI, the MH_{REF} experiments are forced by precessionally enhanced boreal summer insolation and slightly lower greenhouse-gas concentrations (Otto-Bliesner et al., 2017). The prescribed vegetation patterns used in the MH_{GS} experiment are similar to those used by Pausata et al. (2016) and are consistent with the proposed MH vegetation sensitivity experiments in Otto-Bliesner et al. (2017), which involves a substitution of the Sahara desert with evergreen shrubs in the south and steppe and savanna in the north. Moreover, based on the results of Hély et al. (2014), the African Guineo-Congolian rain forest has also been extended slightly northward (Chandan and Peltier, 2020).

160 Each UofT-CCSM4 simulation was separately downscaled over the TP for 15 years, using the WRF model with ~~a~~two nested ~~configuration consisting of an outer and an inner domain.~~domains. The outer domain covers most of Asia at 30-km resolution, ~~while~~and the inner domain ~~encompasses~~covers the TP, as well as parts of the surrounding territory, at 10-km resolution. The outlines of the two domains as well as the topography in the WRF outer domain are shown in Fig. 1. ~~The analysis presented in this article is primarily~~This study is based on a four-member physics ensemble of dynamically

165 downscaled climate simulations, ~~with~~using the same ~~choice of major~~ physics parameterizations as in Huo et al. (2021), where the MH climate anomalies over the South and Southeast Asia were studied. The simulations in each regional climate ensemble employ different cumulus parameterizations in WRF as in Huo et al. (2021), namely the Kain-Fritsch scheme (KF; Kain, 2004), the Grell–Freitas ensemble scheme (GF; Grell and Freitas, 2014), the Tiedtke scheme (Tiedtke, 1989) and the Betts–Miller–Janjić scheme (BMJ; Janjić, 1994), making a mini-physics ensemble for the TP, that allows us to study the

170 sensitivity of model performance to different cumulus parameterizations and thereby to estimate the uncertainty associated with these parameterizations on the simulated MH climate.

The dynamical downscaling methodology ~~employed~~applied here is a somewhat further developed version of the dynamical downscaling "pipeline" originally introduced in Gula and Peltier (2012) and then applied in some more recent studies (d'Orgeville et al~~. (.,~~ 2014~~),;~~; Erler and Peltier~~ (.~~ 2016~~),;~~; Peltier et al~~. (.,~~ 2018~~),;~~; Huo and Peltier~~ (.~~ 2019, 2020, 2021~~) for the~~

175 ~~purpose of investigating~~), where the expected climate change ~~signals~~impacts over the Great Lakes Basin ~~of~~in North America, ~~over western Canada, upstream and downstream of~~along the Rocky Mountains ~~topographic barrier~~, in western Canada and over the South and Southeast Asia~~.~~ were investigated. In the present version of this pipeline, WRF-Hydro V5.1.1 (Gochis et al., ~~2018~~2020) is coupled to WRF for the purpose of performing hydrometeorological simulations. The WRF-Hydro model is a multi-scale and multi-physics hydrologic ~~model~~ community model widely used for flash flood prediction, seasonal

180 simulation of water cycle components and regional hydroclimate impacts assessment both in the short term and long term. In this study, the Noah Land Surface Model (Tewari et al., 2004) is used in the coupled WRF-Hydro modelling system and high-resolution hydrological routing modules have been adopted to represent subsurface lateral flow (Gochis and Chen, 2003). Spin-up simulations of 5 years have also been conducted to achieve numerical stability of the model outputs.

2.2 Observational datasets

185 To ~~validate~~evaluate the historical simulations of ~~historical~~ temperature ~~and precipitation against observations~~, the Climatic Research Unit (CRU) dataset V4.05 (Harris et al., 2020) at 0.5◦ resolution is employed. This widely used climate dataset was derived by the interpolation of monthly climate anomalies from several extensive networks of weather stations. To verify the precipitation results in the historical period, we use both the CRU dataset and APHRODITE's (Asian Precipitation - Highly-Resolved Observational Data Integration Towards Evaluation) gridded precipitation dataset version 1101 (Yatagai et al,

190 2012), which covers Monsoon Asia (APHRO_MA_V1101) at 0.5◦×0.5◦ horizontal resolution. It is a set of long-term (1951 onward) continental-scale daily products that is based on a dense network of rain-gauge data for Asia including the Himalayas, South and Southeast Asia. To compute differences between model results and the observations, the latter have

been reprojected and resampled onto the native grid of each model. However, using these two different observational datasets didn't lead to significant differences to the major results of this study in terms of the validation of precipitation simulation (Fig. 3 and Fig. A1). We have also compared the simulated temperature anomalies during the MH with paleoclimatic reconstructions based on lake sediment (Zhang et al., 2022; Kaufman et al., 2020), and precipitation anomalies with the pollen-based proxy reconstructions by Bartlein et al. (2011) and Herzschuh et al. (2019). Note here for the quantitative reconstructions of Holocene precipitation by Herzschuh et al. (2019), we calculated the averages of all samples from each site within a rather broad time window (5.5–7.45 ka) to represent the MH, in order to be consistent with the method used for calculating the climate anomalies in Bartlein et al. (2011) and to include information from as many points as possible.

In addition, to evaluate the simulated hydrological metrics, mean monthly streamflow data from three stations have been obtained from the Global Runoff Data Centre (GRDC, 2015). These gauging stations (Tanglai Qu, Zhimenda and Yangcun) are located at the basin outlets of the UYEB, UYAB and UBB (Fig. 1) respectively and observations are available from 1978 to 1997, from 1978 to 1997 and from 1956 to 1982, respectively. Not allThere are some missing monthly data in these years in theof station record have complete monthly data; neverthelessrecords; however, all available flowstreamflow data have been used to compute the average monthly discharges discussed in Sect. 4.

3 Historical and MH climates

ThisIn this section presents an overview of the validation of, we first validate our methodology against historical observations as well asthe observational dataset before presenting results from the MH simulations. Note that all temperature and precipitation biases and anomalies reported in this section refer to spatial averageshere are average values over the WRF inner WRF domain, which covers the TP, as well as some surrounding regions.

3.1 Validation against historical observations

Figure 2 shows the JJAS (June-July-August-September (JJAS) and DJF (December-January-February (DJF) temperature biases, compared to the CRU dataset, in the of UofT-CCSM4 historical simulation and in the WRF inner-domain ensemble average for that same time period. The temperature biases are evidently dependent on the season. In JJAS the bias pattern is fairly consistent between the global and the regional models and includes a cold bias over the high elevations of the TP and a warm bias in the northeast of the TP and the lower lands around the TP, especially in the Tarim Basin. Most of the UYEB and UYAB are affected by this warm bias, which will likely reduce summer streamflow due to increased evapotranspiration. Overall, summer temperatures are simulated fairly well by both models and integrated over the entire inner WRF domain, the average temperature bias in both models is less than 0.5∘C. However, during winter, the GCM features a strong cold bias over the TP (> 3∘C averaged over the inner domain), whereas the regional model has a better representation of DJF temperature with a significantly smaller average bias of approximately 1∘C. Among the three river basins, the UBB is most

strongly affected by the cold bias in winter, which may decrease streamflow in the cold season due to late snowmelt. Since

225 most of the precipitation over the TP occurs in summer, Fig. 3 shows the distribution of the JJAS average total precipitation in the observational dataset and the biases in the global model and the WRF ensemble. The spatial patterns in both models and observations are strongly dominated by orographic forcing with very high precipitation intensities on the south side of the Himalayas in contrast with the ~~very low precipitation rates~~small rainfall intensity in the rain shadows ~~of~~behind the ~~mountain ranges, in particular~~high mountains, especially over the northern TP which ~~constitutes a major part of~~covers both

230 the UYEB and UYAB. There is moderate rainfall over the Sichuan Basin east of the TP, and the southern plateau, where the UBB is located. ~~However,~~It is evident that the representation of orographic precipitation ~~is strongly dependent~~relies on model resolution: the ~~low~~coarse-resolution ~~global model significantly underestimates both the~~UofT-CCSM4 shows a severe underestimation of the peak intensities in front of the Himalayas ~~as well as~~and an overestimation of the ~~rain shadow effect~~precipitation rates in ~~its lee.~~the northern TP. The representation of ~~orographic impact on~~ precipitation is

235 ~~dramatically~~greatly improved in WRF at 10-km resolution. The wet bias over the northern and eastern TP has also been eliminated in the RCM. Averaged over the WRF inner ~~WRF~~ domain, the JJAS precipitation bias is 0.4_9_ mm d^{-1} in the WRF ensemble average and 1.4_7_ mm d^{-1} in the driving UofT-CCSM4 simulation. The overestimation in precipitation over the western and south-eastern TP in WRF is also accompanied by lower surface temperature, which is likely related to the greater cloud cover reflecting more shortwave flux at high levels. Both models show a similar wet bias in winter (Fig. 3d~~),~~)

240 and such excessive snow in winter possibly contributes to the lower ~~winter~~DJF temperature (Fig. 2) through snow–albedo feedback.

3.2 Simulated MH climate

We next turn to an attempt to analyse the climate anomalies in MH$_{REF}$ and MH$_{GS}$ and to investigate the impact of the Saharan vegetation on the TP.

245 The simulated JJAS temperature over the TP in our MH ensembles is shown in Fig. 4. ~~Due~~Owing to the ~~change~~variation in the Earth's orbital ~~parameters~~configuration, during the MH ~~the NH receives more~~ summer insolation ~~during boreal summer that leads to~~in the NH was stronger than today, resulting in a significant warming over the TP in both the GCM and the WRF ensemble (Figs. 4a and 4b). The temperature response also shows cooling south of the TP and over the ocean (Huo et al., 2021). Thus, the land-sea thermal contrast is increased in the MH favouring the enhancement of the monsoon circulations.

250 The winter temperature over the TP shows a general cooling over the TP (Fig. 4e) that is associated with the decrease in winter ~~insolation in the NH. These changes imply that the solar radiation is one of the most important factors dominating the temperature changes in climate models.~~solar radiation. Comparing the JJAS temperature changes produced by the GCM and RCM, the WRF ensemble shows an overall stronger warming over the TP, particularly in the northern part. Moreover, the regional model also produces a larger warm anomaly than the global model from mid-summer to early-winter (Fig. 4e).

255 Taking the influence of a vegetated Sahara into account results in higher temperature over the TP all year round, except in winter when the difference is negligible (Figs. 4d and 4e). The influence of MH$_{GS}$ in both models is characterized by an

overall increase in the annual mean temperature over the TP, which agrees with estimates from pollen records (Shi et al., 1993), while an annual cooling is obtained with MH$_{REF}$. Averaged over the WRF inner domain, the JJAS temperature anomalies of the WRF ensemble mean are 1.1 ∘C with MH$_{REF}$ and 1.8 ∘C with MH$_{GS}$. Particularly, over the norther plateau,

260   the warming is significantly enhanced from approximately 2 ∘C to 4 ∘C, leading to a better agreement with proxy-based estimation of 4–5 ∘C warming (Shi et al., 1993) over the TP. Moreover, compared to paleoclimatic reconstructions based on lake sediment in Fig. 4 (Zhang et al., 2022; Kaufman et al., 2020), both MH experiments generally capture the summer warming trend over the TP. In south-eastern TP, there is a good agreement between the model simulations and the reconstructions. The simulated temperature anomalies in MH$_{GS}$ fit the reconstructed paleoclimatic records in the north-

265   eastern and south-central TP better but overestimate the warming signal over the central-eastern part of the TP (Fig. 4d). Meanwhile, the two proxy data points located in the central-western TP west of the 85° W indicate strong cooling (< –4 ∘C) during the MH, which disagrees with all model simulations. Note here these two records are from frozen lakes, where the reconstructed temperature records reveal air temperature changes during the ice-free season (May - September), not just JJAS. Also note here all proxy records are subject to uncertainties that arise from the dating processes (Wang et al., 2021)

270   and site-specific factors like the change in vegetation cover and the retreat of glaciers (Chen et al., 2020a). Averaged over all the points except these two, both UofT-CCSM4 and the WRF ensemble average have a bias of –1.2 ∘C in MH$_{REF}$. Inclusion of a GS greatly reduces this cold bias to –0.1 ∘C in WRF, which is also smaller than that of the global model in MH$_{GS}$ (–0.4 ∘C).

MH orbital and ~~GHG~~greenhouse gas forcings result in wet anomalies in both global and regional models (Figs. 5a and 5b).

275   The enhanced annual precipitation in the southern parts of the TP in MH$_{REF}$ broadly agrees with ~~the proxy~~ reconstructions ~~by~~ (Bartlein et al.~~., 2011) and~~; Herzschuh et al.~~., 2019). However, with orbital forcing alone (MH$_{REF}$) both models fail to reproduce the wet anomaly in the east and southeast parts of the TP, although the area with reduced rainfall in the downscaled results is smaller than that in UofT-CCSM4 and thus agrees better with the overall wet signal suggested by reconstructions. ~~Considering~~Averaged over all the points ~~with~~that have proxy data from Bartlein et al. (2011)/Herzschuh et

280   al. (2019) within the ~~WRF~~ inner domain, the WRF ensemble average has a bias of –0.~~664~~/–0.19 mm d^{-1}, which is slightly smaller than that of the global model (–0.~~7~~73/–0.23 mm d^{-1}). Under GS forcing (MH$_{GS}$), precipitation is simulated to increase over almost the entire domain except a small patch in the southeast (Fig. 5d). The inclusion of GS surface boundary conditions greatly expands and intensifies the wet anomalies in WRF, further reducing the dry bias with respect to the ~~reconstruction by~~ pollen-based reconstructions (Bartlein et al.~~., 2011) by half. The bias produced by the global model,

285   however, only sees a small decrease from –0.73 mm d^{-1} to –0.71 mm d^{-1}, mainly due to the dry bias over the eastern part of the TP (Fig. 5c). Compared to the reconstructed precipitation anomalies from Herzschuh et al. (2019), WRF also has a much smaller bias (0.02 mm d^{-1}) than the global model (–0.12 mm d^{-1}) in MH$_{GS}$. Reconstructions based on lacustrine sediments (Shi and Song, 2003; Sun et al., 2006) ~~suggested about 20–50% higher~~implied an annual precipitation increase of 20–50% over ~~Daihai Lake (113∘ E, 41∘ N) and~~ Diaojiao Lake (112∘ E, 41∘ N) and Daihai Lake (113∘ E, 41∘ N) during the MH. WRF

290   produced precipitation increases of 38% and 30% at these two locations when the influence of a vegetated Sahara is

9

considered, which ~~agrees~~is consistent with the ~~range of~~ reconstructed ~~precipitation~~rainfall changes. However, the ~~precipitation~~ increase rates at these two locations are significantly underestimated by both UofT-CCSM4 in MH$_{GS}$ (Fig. 5c; less than 20%) and the WRF simulation without GS forcing (Fig. 5b; less than 5%). Comparison of downscaled results including the GS with paleoclimate reconstructions shows significant improvements, especially over the north and west sides of TP. These results highlight the climate sensitivity to Saharan vegetation changes via ocean-atmosphere teleconnections and emphasized the importance of incorporating MH vegetation feedbacks.

The spatial patterns of JJAS precipitation anomalies resemble those of the annual mean but with a larger magnitude (Fig. 6), which is expected since annual precipitation largely results from the summer rainfall over the TP, a region heavily influenced by the Asian monsoon circulation. The seasonal cycle of precipitation obtained with MH$_{REF}$ changes in response to the insolation changes at 6 ka (Fig. 6c): rainfall slightly decreases before May and then strengthens with the onset of the monsoon. ~~Meanwhile~~Besides, the ~~retreat of~~ monsoon withdrawal is also delayed by ~~about~~ one month as the increased rainfall persists ~~until~~till October. Such changes are consistent with the results obtained in PMIP models (Zheng et al., 2013). Inclusion of the GS boundary conditions not only leads to a weaker decrease in rainfall than MH$_{REF}$ in spring, but also eliminates the negative rainfall anomaly in May in MH$_{REF}$. During the monsoon season (JJAS), the precipitation increases in MH$_{GS}$ are more than two times as large as those ~~caused by the MH orbital and GHG forcings alone~~in MH$_{REF}$ in both the UofT-CCSM4 and WRF physics ensemble members over the TP. Averaged over the WRF inner domain, JJAS precipitation is generally found to increase by 0.5 mm d^{-1} (14%) in MH$_{REF}$ and 1.1 mm d^{-1} (31%) in MH$_{GS}$ in the WRF ensemble average. Comparing different WRF ensemble members, they all share similar general characteristics, but the magnitude of the absolute precipitation changes depends on the individual ensemble member (Figs. 6c and 6f). The fourth ensemble member ~~using~~based on the BMJ cumulus scheme produces the smallest ~~absolute~~increase in JJAS precipitation ~~increases~~ in both MH$_{REF}$ (0.35 mm d^{-1}) and MH$_{GS}$ (0.87 mm d^{-1}) experiments, while the KF scheme ~~in~~ (the first ensemble member) and the GF scheme ~~in~~ (the second ensemble member) produce the ~~largest~~greatest rainfall ~~increase~~increases in MH$_{REF}$ (0.59 mm d^{-1}) and MH$_{GS}$ (1.31 mm d^{-1}), respectively. The ~~Sahara~~greening of the Sahara also intensifies the precipitation ~~at~~over the ~~end of the monsoon season (~~TP in September and October~~) over the TP~~, further postponing the retreat of the monsoon ~~withdrawal~~, which is similar to the findings in our previous studies over South and Southeast Asia (Huo et al., 2021).

The enhanced precipitation in MH experiment with Saharan vegetation is probably owing to ocean-atmosphere teleconnections as suggested in previous studies (Huo et al. 2021; Pausata et al., 2017). An albedo-induced warming develops over the vegetated Sahara, leading to a strong intensification and northward expansion of the West African Monsoon and a significant tropical North Atlantic SST warming (Fig. 7b; Pausata et al., 2016), which in turn changes atmospheric circulation and induces a notable intensification and westward extension of the Walker Circulation over the Pacific Ocean in the MH$_{GS}$ (Fig. 7d) compared to the MH$_{REF}$ experiment (Fig. 7c). The changes in the Walker Circulation weakens the low-level easterly winds over the eastern Pacific, but enhances easterly anomalies over the northern Indo-Pacific Ocean (Fig. 7b), which suppresses ENSO activity and enhances the Asian monsoon (Pausata et al., 2017).

4 Three river basins

325 In this section, the simulated climate for the present day as well as the MH over the three river basins on the TP are discussed. ~~The hydroclimatic analysis presented here are based on surface fluxes and climatic state variables averaged over each river basin. Figures 7, 9 and 11 show the seasonal~~Figures 8-10 present the annual cycles of hydroclimatic variables over the UYEB, UYAB and UBB during the historical period and Figs. ~~8, 10~~11 and 12 show the anomalies during the MH. In ~~these figures~~Fig. 8-10, the WRF ensemble averages are plotted in thick black lines while results from individual ensemble

330 members are plotted in colors (see figure legends). ~~All variables were averaged over the entire basin area and over each 15-year simulation period. Observations are shown~~The error bars on the observational data in Fig. 8-10 represent the standard error of the mean and the error bands in Figs. 11 and 12 shows the distribution range for all ensemble members. All hydroclimatic variables have been averaged over the corresponding river basin. Observational results in Fig. 8-10 are represented by open circles. Only temperature, total precipitation, and river discharge are available from observations. The

335 observed temperature ~~and~~ (precipitation) values ~~have been assembled~~are from ~~gridded~~ CRU ~~observational datasets and averaged over the area of the basins~~(APHRODITE) dataset. The river discharges, recorded by gauging stations, have been normalized by the associated basin area. Areas of contribution for UYEB, UYAB and UBB are approximately 286000 km^2, 138000 km^2 and 153000 km^2, respectively. ~~The error bars on the observational data are based on the standard error of the mean (SEM), which is defined as $\sigma/\sqrt{n}$, where σ is the sample standard deviation and n is the sample size.~~

340 Solid precipitation in panel b of Figs. ~~7 12~~8-11 is snow and graupel, and net precipitation (panel c in Figs. ~~7 12) is defined as~~8-10 and Fig. 12) is calculated by subtracting evapotranspiration from total precipitation ~~minus evapotranspiration~~. Note that evapotranspiration, snowfall, and snowmelt are calculated by the Noah land surface model, while ~~runoff~~streamflow is computed by the WRF-Hydro model.

For comparison between the preindustrial and MH simulations, we applied the linear scaling method to the original

345 streamflow results. Due to the large (negative) JJAS runoff bias in WRF during the historical period, especially in the UYEB and UYAB (Figs. 7d and 9d), it was deemed necessary to apply a simple form of bias correction to rescale the monthly river discharge so that the monthly watershed average for the historical period matches the observations (using one factor per month). Linear scaling corrects the ensemble mean values of the historical simulations based on monthly errors (Trambauer et al., 2015). The scaling factor was first obtained through calculating the ratio between the observed and modelled historical

350 values. Then the monthly scaling factor was applied to each uncorrected daily runoff simulations of that month so that the monthly mean values of the historical simulations match those of the observation. The streamflow values of the MH simulations have been bias corrected using the same factors as for the historical results so that they can be usefully compared.

4.1 Validation of the average season cycle of hydroclimatic variables

355 The seasonal cycles of hydroclimatic variables over the three river basins are provided in Figs. 8-10. The Yellow River originates in the northern TP and ~~runs~~flows eastward ~~across~~through the Loess Plateau and the North China Plain, eventually draining into the Pacific Ocean at the Bohai Gulf on the east coast of China. The UYEB above the Tanglai Qu hydrometric station, with an altitude varying from 4.9 km in the southwest to 1.1 km in the northeast, is situated on the northeast side of the TP but also covers a small section of the western Loess Plateau (Fig. 1). It has over 400 mm annual rainfall according to

360 the APHRODITE dataset and an annual mean temperature of approximately 2 ∘C based on the CRU dataset. The UYAB lies in the eastern part of the TP and is influenced by the Asian monsoon. The basin, whose altitude varies from 5.7 km in the west to 4.2 km in the east, drains past the Zhimenda hydrological station (Fig. 1). The integrated precipitation in JJAS accounts for more than 85% of the total annual precipitation (Fig. 9b) and the JJAS discharge accounts for more than 70% of the annual total at Zhimenda (Fig. 9d). The Brahmaputra River originates from the Himalayas and passes through the

365 southern TP before it breaks through the eastern Himalayas and turns southward. Elevation of the UBB, above the Yangcun hydrometric station ranges between 5.8 km and 3.8 km and drops off from the west to the east. ~~It is situated within a semiarid region with an annual precipitation of approximately 400 mm and an annual mean air temperature of approximately 2 ∘C based on the CRU dataset~~Based on the observation, the basin-averaged annual precipitation is 314 mm and the annual mean temperature is −1 ∘C.

370 The seasonal ~~cycles of hydroclimatic variables over the UYEB are provided in Fig. 7. With the exception of winter, the seasonal~~ cycle of air temperature ~~(Fig. 7a)~~ is ~~very~~generally accurately reproduced ~~by the WRF ensemble. The GCM temperature is lower than the observation by 3.8 ∘C in DJF but the WRF model is able to reduce this~~ over the three river basins, except for a cold bias ~~to approximately 1.4 ∘C.~~during winter, even though the downscaled simulations have already halved the DJF cold bias in the global simulation. The large cold bias in UofT-CCSM4 is likely due to excess winter

375 precipitation (~~Fig. 7b) combined with delayed snowmelt,~~panel b in Figs. 8-10), which results in a snow–albedo feedback on temperature. It is interesting to note that the WRF ensemble actually suffers from a stronger cold bias than the UofT-CCSM4 in spring over the two cooler basins (UYAB and UBB), which is likely associated with the poor representation of snowmelt processes by the much simpler snow model employed in WRF. The JJAS temperatures simulated by both the global and the regional models fit the observation well.

380 The Asian monsoon exerts strong influence on the ~~UYEB: about~~three river basins over the TP: over 70% of annual precipitation ~~falls in JJAS and less than 2%~~occurs in JJAS and only about 10% falls in the winter ~~months~~ (DJF) according to the observation. The simulated seasonal cycle of precipitation in WRF is too strong compared to the observation~~, owing~~ over the UYEB and UBB, largely due to ~~excessive precipitation~~the rainfall overestimation in summer (~~the wettest~~wet season). This bias is inherited from the GCM and although downscaling greatly reduces the bias, precipitation is still overestimated

385 for JJAS ~~over~~. Over the ~~UYEB~~UYAB, qualitatively the annual precipitation pattern is well reproduced by the WRF

ensemble, while UofT-CCSM4 is characterized by a much greater wet bias, with significantly more precipitation in spring and summer (Fig. 7b).9b). The improvement in simulation of both regional temperature and precipitation by WRF indicates the fidelity brought by the use of higher resolution. There is, as expected, little solid precipitation in summer and all precipitation falls asin solid precipitation form during winter, which leads to a in UYEB, resulting in a streamflow peak

390   driven by snowmelt driven runoff peak in late spring and early summer (Fig. 8c). Summer precipitation also primarily falls as liquid rain in UYAB and UBB, but there is still snow even in July and August because of the colder climate over these two basins compared to the UYEB and snowfall in UBB is in fact relatively evenly distributed throughout the year. Note here7c). It is interesting to note that the spread among the ensemble members is significantly larger for liquid precipitation than for solid precipitation or temperature; different convection schemes greatly affect the JJAS precipitation and the second

395   ensemble member using the GFEGF cumulus scheme exhibits the largest wet bias. Net over the two basins in the northern TP whereas the BMJ scheme produces the largest excess in precipitation over the UBB.

The seasonal cycle of net precipitation pattern is characterized by in UYEB and UYAB has two peaks in (June and September), due to the large evapotranspiration in July and August (Figs. 8c and 9c). Snowmelt over these tow basins is also characterized by double peaks, which correspond to the two peaks in snowfall (Figs. 8b and 9b). Therefore, the melting of

400   fresh snowfall is likely the major contributor to the snowmelt peaks simulated by the model. Over the UBB, although both observed and simulated total precipitation starts to increase in June, net precipitation is small in early summer due to evapotranspiration (Fig. 11c). Net precipitation from the first WRF ensemble member with the KF cumulus scheme is in fact negative in May and June. 7c).Runoff over the UBB starts to increase in May (Fig. 10d), which possibly comes from the snowmelt contribution that is the largest in May and June (Fig. 10c). In UBB, the runoff maximum over the UBB in August

405   coincides with the largest net precipitation rates in July and August, which indicates that UBB rainfall plays a dominant role in peak runoff during the after-snowmelt seasons. The seasonal streamflow for the UYEB during the historical period for the two basins in the north exhibits a broad shape with flow increasing slowly in April and slowly declining after October. Runoff in spring and early summer clearly follows the timing of snowmelt. Streamflow regime is also characterized by double peaks, in July and September, respectively (Fig. 7d). The Figs. 8d and 9d). Over the UYEB, the good correspondence

410   between the streamflow timing of the peaks of runoff and net precipitation regimes in summer suggestsSeptember indicates that the monsoon rainfall is the dominant contributor to runoff streamflow for UYEB. However, over the UYEBUYAB, both snowmelting and precipitation contribute to the second runoff peak in September. WRF-Hydro is able to reproduce runoff that broadly agrees with observed river discharge. However, the model tends to underestimate the magnitude of the runoff peaks. This is likely a result of the stronger evapotranspiration, leading to a lower runoff.

415   The mismatch in streamflow peak magnitude against the observation is similar in all WRF simulations based on different physics configurations except the second ensemble member using the GF cumulus scheme; the GF cumulus scheme overestimates the runoff all year round and also produces the largest net precipitation and snowmelt among all four WRF ensemble members.

4.2 Simulated MH changes

420 During the MH, the overall changes in mean temperature ~~in the UYEB~~(Fig. 11a-c) follow changes of insolation the magnitude of which increases during boreal summer and decreases in winter. The WRF model produces <u>significantly</u> larger positive temperature anomalies in ~~late~~ summer ~~and smaller cold anomalies in fall over the UYEB~~ compared to UofT-CCSM4 ~~(Fig. 8a).~~. Compared with MH_{REF}, temperature changes in experiments with the GS forcing have very similar characteristics, but the simulated temperature is generally warmer than in MH_{REF} ~~(Figs. 8a~~<u>over all river basins in both global</u>

425 ~~and 8b).~~<u>regional models.</u> Warming also starts earlier in May ~~instead of June~~ and ends one month later in November and the peak warming also occurs one month later in <u>early autumn in</u> our WRF MH_{GS} experiments relative to the MH_{REF}. ~~Both the sign and magnitude of the~~<u>In both MH ensembles, different WRF configurations show very similar</u> temperature changes ~~are similar between the WRF simulations based on different physics configurations in both MH ensembles.~~.

The changes in monthly precipitation ~~over UYEB~~ are shown in ~~Figs. 8c and 8d.~~<u>Fig. 11d-f.</u> The MH_{REF} simulations ~~in~~<u>for</u> both

430 ~~UofT-CCSM4~~<u>UYEB</u> and ~~WRF~~<u>UYAB</u> show a significant decrease in precipitation except in ~~September and October.~~<u>autumn.</u> The absolute regional dry anomaly is the largest in August, while September <u>(October)</u> experiences the largest increase in rainfall~~-~~ <u>in the UYEB (UYAB).</u> When vegetation is imposed over the Sahara, the ~~negative peak~~<u>minimum</u> in August and the ~~positive peak~~<u>maximum</u> in September <u>(October)</u> still exist, but there is another smaller precipitation increase peak in June~~,~~ <u>(July),</u> showing a strong rainfall enhancement ~~in late spring and~~<u>during the</u> early monsoon season in response to the GS

435 forcing. However, averaged over the whole monsoon season, the WRF ensemble mean in MH_{GS} ~~shows no significant precipitation change (< 3~~<u>only shows a small increase over these two basins (~ 5</u>%) due to the offset between these positive and negative anomalies, while the WRF simulations that only account for the insolation forcing (MH_{REF}) produce a decrease in monsoonal precipitation (9%). Another major change ~~in~~<u>to</u> the ~~hydrological cycle of~~<u>hydroclimate over</u> the UYEB <u>and</u> <u>UYAB</u> is the shift of part of the solid precipitation to liquid form in ~~spring and~~ summer in MH_{GS} when compared to MH_{REF}~~,~~

440 <u>(Fig. 11d and e),</u> which <u>will</u> in turn ~~will lead to~~<u>result in</u> a ~~decline in~~<u>decreased</u> snowmelt ~~(Figs. 8e and 8f). The~~<u>Fig. 12a and b).</u> <u>Over the UBB, annual precipitation in the both MH experiments increases (~0.15 mm d^{-1} or 11% increase for MH_{REF} and 0.35 mm d^{-1} or 26% increase for MH_{GS}), which is larger than those over the other two basins. However, although the increasing trend is robust among all WRF ensemble members, the magnitude of the increase is subject to higher model uncertainties than the other two basins. Compared to the increase in total precipitation, there is little change in snow amount</u>

445 <u>for both MH experiments (< 0.04 mm d-1) over the UBB, which also leads to very small changes in the annual snowmelt (Fig. 12c). Over the other two basins, however, the</u> reduction in peak snowmelt due to the combined effects of MH insolation forcing and GS forcing is ~~close to 50%.~~<u>over 30% (Fig. 12a and b).</u> At the same time higher temperatures during the warm season resulting from the MH insolation forcing also lead to larger evaporation, which accounts for the drop in net precipitation and also the <u>substantial</u> decrease ~~of the UYEB~~<u>in</u> discharge especially in summer (~~Figs. 8g~~<u>Fig. 12d</u> and ~~8h~~<u>e</u>).

450 The magnitude of streamflow reductions in ~~both MH experiments are similar~~<u>slightly larger in MH_{GS} than MH_{REF}</u>, a consequence of the ~~larger~~<u>higher</u> temperature ~~rise in MH_{GS}~~ and ~~the opposite and compensating effects of larger snowmelt and~~

14

less snowfall in MH$_{GS}$, which leads to greater evaporation, ~~though the peak of streamflow~~ and less snowmelt. Compared with UYEB, the reduction in snowmelt plays a more important role in the runoff decrease ~~in MH$_{GS}$ occurs one month later compared to the MH$_{REF}$ in late monsoon season (September).~~ over the UYAB. Such reduction in the upper Yellow River runoff has also been found over the past decades, which is related to rising temperatures and decreasing wet season precipitation (Cuo et al., 2013).

~~4.2~~ The ~~UYAB~~

~~The UYAB lies in the eastern part of the TP and is influenced by the Asian monsoon (Fig. 1). The basin, whose altitude varies from 5.7 km in the west to 4.2 km in the east, drains past the Zhimenda hydrological station (Fig. 1). The integrated precipitation in JJAS accounts for more than 85% of the total annual precipitation (Fig. 9b) and the JJAS discharge accounts for more than 70% of the annual total at Zhimenda (Fig. 9d).~~

~~Figure 9 shows the seasonal cycles of basin temperature, precipitation, snowmelt and streamflow in the UYAB. It is evident that the seasonal cycle in temperature is quite well reproduced, except for a larger cold bias in winter than the UYEB, even though the downscaled simulations have already halved the DJF cold bias in the global simulation. It is interesting to note that the WRF ensemble actually suffers from a stronger cold bias than the UofT-CCSM4 in spring (−3 °C in March-April-May). Note here, UYAB covers a relatively smaller area, compared to other basins, and the station density in the UYAB is relatively low (Harris et al., 2020), so that the observational error can be large. Like the UYEB, precipitation in the UYAB peaks in summer and is relatively low in winter (Fig. 9b); qualitatively the seasonal cycle is well captured in WRF, but the contrast between summer and winter is still overestimated in all WRF ensemble members. In all WRF ensemble members, the seasonal precipitation over the UYAB is somewhat better represented in the third WRF ensemble member with the Tiedtke cumulus scheme whereas the GFE scheme used in the second ensemble member produces the largest excess in JJAS precipitation. UofT CCSM4, however, is characterized by a much greater wet bias, with significantly more precipitation in spring and summer. The improvement in simulation of both regional temperature and precipitation indicates the fidelity brought by the use of higher resolution. From December to April, all precipitation occurs as snow. In summer, precipitation primarily falls as liquid rain, but there is still snow even in July and August because of the colder climate over the UYAB compared to the UYEB. Snowmelt over the UYAB is again characterized by two peaks in June and September (Fig. 9c), which correspond to the two peaks in snowfall (Fig. 9b). Therefore, the melting of fresh snowfall is likely the major contributor to the snowmelt peaks~~ simulated ~~by the model. Even though the simulated precipitation maximum in the UYAB occurs in August, the net precipitation peaks in September due to the great evapotranspiration in August (Fig. 9c). The observed streamflow in the UYAB rapidly rises in June and reaches a maximum in July, and flow level remains relatively high until September (Fig. 9d). The monthly streamflow during the historical period was reasonably simulated by the WRF-Hydro model, but there is significant underestimation of streamflow in July and August (Fig. 9d). This is likely a result of the stronger evapotranspiration, leading to a lower runoff. The mismatch in runoff peak magnitude compared to observed streamflow is similar in all WRF configurations except the second ensemble member using the GFE cumulus scheme; the~~

15

GFE cumulus scheme overestimates the runoff all year round and also produces the largest net precipitation and snowmelt among all four WRF ensemble members.

The changes to the surface air temperatures in UYAB during the MH are also determined by the changes to the pattern of insolation (Figs. 10a and 10b). In both MH$_{REF}$ and MH$_{GS}$ experiments, the temperature anomalies produced in WRF are larger than the UofT CCSM4 all year round, especially in fall. During the MH, temperature is simulated to have increased by 1.6 °C in the monsoon season in the WRF ensemble average in MH$_{REF}$ (compared to 1.0 °C in UofT CCSM4), and 3.1 °C in MH$_{GS}$ (compared to 2.2 °C in UofT CCSM4). In comparison, the ensemble mean for the MH experiments which assumes the same Saharan vegetation cover as the PI experiences a small annual cooling over the UYEB (−0.2 °C), while including a green Sahara flips the annual temperature anomaly into a warming of 1.3 °C. JJAS precipitation changes in the WRF ensemble mean are −9.8% in MH$_{REF}$ and 5.3% in MH$_{GS}$ (Figs. 10c and 10d), and such a transition from a dry to a wet anomaly is clearly associated with the strengthening of the Asian monsoon resulting from the greening of the Sahara (Pausata et al., 2017; Huo et al., 2021). UofT CCSM4, on the other hand, simulates almost no change in summer precipitation for the UYAB in MH$_{REF}$ and a much larger increase in the MH experiment with a vegetated Sahara. However, considering the far superior representation of summer precipitation in WRF as opposed to UofT CCSM4 (Figs. 3 and 9), we suggest that this may in fact be an artifact of the low resolution employed in the GCM. Note, however, that because of the relatively smaller size of the basin, total precipitation changes over UYAB have a larger spread between the WRF ensemble members than in UYEB, but the temperature induced change from solid to liquid precipitation and in particular the snowmelt decline for most months are very robust among all WRF ensemble members (Figs. 10e and 10f). The reduction in annual snowmelt in the WRF ensemble is approximately 17% in MH$_{REF}$ and 19% in MH$_{GS}$. These changes combined with the generally increased evaporative water losses cause a substantial decrease in runoff, especially in summer (Figs. 10g and 10h). Such negative anomaly in JJAS discharge of the upper Yangtze River also agrees with CMIP5-based projections (Krysanova et al., 2017) and hydrological model results forced by PMIP4 data during the last interglacial (LIG; Scussolini et al., 2020). Compared with UYEB, the reduction in snowmelt plays a more important role in the runoff decrease over the UYAB. The magnitudes of UYAB runoff changes in both MH simulations are similar because the greater net precipitation in summer in MH$_{GS}$ is largely compensated by reduced snowmelt.

4.3 The UBB

The Brahmaputra River originates from a glacier at an elevation of 5.8 km in the southwest Himalayas and flows through the southern TP before it breaks through the eastern Himalayas and turns southward. 2020). Among the three basins, one major difference in the hydroclimate over the UBB Elevation of the UBB, above the Yangcun hydrometric station ranges between 5.8 km and 3.8 km and drops off from the west to the east. Note that the UBB lies in a wetter region than the UYEB and UYAB, and the average precipitation rate is much higher (Fig. 3a), so that the basin-integrated water flux is also larger. The seasonal cycle of hydroclimatic variables from the GCM and the WRF ensemble for the UBB is shown in Fig. 11. Based on the observation, the basin-averaged annual precipitation is 741 mm and the annual mean temperature is −1 °C. The global

16

model has a year-round cold bias, which is particularly severe in winter. The general representation of the temperature seasonal cycle is significantly improved in the WRF ensemble where the DFJ cold bias is reduced by half. However, the WRF ensemble has a larger cold bias than the global model in spring, which is likely associated with the poor representation of snowmelt processes by the much simpler snow model employed in WRF. The winter precipitation is well capture in the WRF ensemble, while summer precipitation is somewhat underestimated. The global model is, however, characterized by a wet bias in all seasons. Note here that the station density in parts of the UBB is very low, so that the observational error can also be large (Harris et al., 2020). All of the precipitation from November to April falls in solid form, which leads to a snowmelt peak in late spring and early summer. Unlike UYEB and UYAB, snowfall in UBB is more evenly distributed throughout the year. In observations as well as in our simulations, total precipitation starts to increase in June, but net precipitation is small in early summer due to evapotranspiration (Fig. 11e). Net precipitation from the first WRF ensemble member with the KF cumulus scheme is in fact negative in May and June. However, runoff over the UBB starts to increase in May (Fig. 11d), which possibly comes from the snowmelt contribution that is the largest in May and June (Fig. 11e). In UBB, the JJAS flow accounts for approximately 70% of the annual total according to observations obtained at the Yangcun station. The peak flow in the UBB occurs in August, consistent with the highest net precipitation in July and August, which indicates that UBB rainfall plays a dominant role in annual total surface runoff. The underestimation in the simulated peak streamflow is most likely due to the underestimation of precipitation over the basin. The first WRF ensemble member, which produces the greatest runoff underestimation, also has the largest negative bias in JJAS precipitation.

During the MH, annual mean temperature is simulated to drop by approximately 0.7 °C in the WRF ensemble in response to orbital forcing alone (Fig. 12a) and rise by 0.7 °C in experiments that account for a vegetated Sahara (Fig. 12b). UofT-CCSM4 also shows a similar shift from negative to positive temperature anomalies when the greening of the Sahara is taken into consideration. In both WRF MH experiments, the warming appears to be more pronounced at the end of the monsoon season (September and October). The average JJAS warming is 0.5 °C in MH$_{REF}$ and 1.5 °C in MH$_{GS}$. On average, annual precipitation in the WRF ensemble increases by approximately 0.15 mm d^{-1} for MH$_{REF}$ (i.e. 11% increase with individual ensemble members ranging from 3%–17%) and 0.35 mm d^{-1} for MH$_{GS}$ (i.e. 26% increase with an ensemble range of 19%–37%). Both MH experiments show a significant increase in precipitation in JJAS after a small decrease in late winter–early spring and little change in precipitation is seen in November and December. Compared to the increase in total precipitation, the change in the total amount of snow is very small for both MH experiments (< 0.04 mm d^{-1}), which also leads to very small changes in the annual snowmelt. A major change in the basin hydrology is the increase of net precipitation in JJAS, which also results in an overall increase in runoff. In MH$_{REF}$, streamflow first decreases very slightly in April and May and June and then increases in the second half of the year with peaks occurring starts to increase in July. In WRF simulations that consider the influence of the Sahara greening, runoff still exhibits similar increasing trends betweenfrom July andto September, which is consistent with changes in precipitation, but little changethere is detected for runoff in the first half of the year. The overall river discharge increasing trend over the UBB is robust across the WRF ensemble (~27% in ensemble average ofno decrease in May, probably due to the enhanced snowmelt compared to MH$_{REF}$ and ~55% in MH$_{GS}$), but the

17

555 Similar river runoff increase has also been found in future projections in a warmer climate using a hydrological model and multi-source spatial data (Cai et al., 2017) and LIG hydrological simulations based on PMIP4 data (Scussolini et al., 2020).

5 Summary ~~and conclusions~~

~~We have presented~~Using dynamically downscaled high-resolution climate simulations ~~for~~over the TP, ~~with an analysis of~~this study analyses the hydroclimate in three major river basins, the UYEB, UYAB and UBB. ~~The fully coupled~~ Climate

560 simulations constructed using the UofT-CCSM4 global climate model ~~UofT-CCSM4 was used to generate climate simulations~~ for the modern and MH time periods~~, which~~ were dynamically downscaled to ~~a~~10-km resolution ~~of 10 km~~, using coupled WRF-WRF-Hydro with four different cumulus parameterization schemes. Compared to the GCM, WRF is far superior in representing orographic precipitation and the ~~variation across the seasonal cycle.~~annual cycles of hydroclimatic variables. It captures the sharp contrast between the very high precipitation rates south of the Himalayan Mountain ranges

565 and the dry climate ~~in their rain shadows~~ over the interior plateau. Both ~~UofT-CCSM4~~global and ~~WRF configurations~~regional models suffer from a winter cold bias ~~in winter due~~owing to excessive snowfall, but the regional model has again significantly reduced this cold bias.

The coupled UofT-CCSM4-WRF-WRF-Hydro model has also been ~~used~~employed to investigate the ~~changes in~~ temperature and precipitation changes over the TP during the MH. Both the GCM and the WRF ensemble average show a warming ~~over~~

570 ~~the TP during the boreal~~in summer and a cooling in winter over the TP, which ~~results from~~is probably induced by insolation change. As far as the JJAS temperature is concerned, the WRF simulations show a larger warming than that in the driving global model, especially in the northern part of TP, and is thereby closer to estimates from ~~pollen~~proxy records ~~(Shi et al., 1993).~~. The ~~enhanced land-sea~~strengthened thermal contrast between continent and ocean during summer ~~favours the strengthening of~~enhances the monsoon circulation, ~~featuring~~leading to stronger ~~southerly winds from the sea, which in turn~~

575 ~~enhances the~~northward ~~water vapour~~winds, as well as stronger moisture transport~~.~~ from the sea. The ~~general~~spatial patterns for the ~~changes of~~TP precipitation change are generally similar in sign between the GCM and the RCM, with significant increase in the southern parts of the TP. The ~~seasonal~~ annual precipitation cycle ~~of rainfall~~over the TP is ~~modified~~changed by the ~~change of~~insolation anomalies during the MH, such that precipitation weakens slightly ~~in spring~~before the monsoon season and strengthens ~~during the summertime~~in summer. The annual wet anomalies are stronger and more extensive in the

580 downscaled simulations and thus fit better with the proxy data. Since the TP plays a profound role in the development of the Asian monsoon and heavy precipitation forms when the wind from the sea rises along the south and east edges of the plateau, the model's ~~abilities in~~ability to realistically ~~representing~~represent the ~~huge~~complex steep topography may have a great impact on the coupling between the ~~changes over the TP and the~~ general monsoon circulations~~.~~ and the regional changes

18

over the TP. Including a ~~green Sahara~~GS further strengthens the TP precipitation and ~~halves~~significantly reduces the bias against reconstructions over the TP, which highlights the significance of the teleconnections between the Saharan vegetation and the TP in paleoclimate simulations. Saharan vegetation plays a crucial role in intensifying the West African Monsoon and modulating the atmospheric circulation, which alters the Walker circulation and increases Asian monsoon precipitation, through changes in equatorial Atlantic SSTs (Fig. 7). Precipitation changes in MH experiments which assume preindustrial vegetation cover are ~~to a good approximation about~~approximately half the magnitude of ~~changes~~those in MH$_{GS}$ in all WRF ensemble members, although there are notable differences in the simulated MH rainfall anomalies using different physics schemes.

Both UYEB and UYAB hydrological regimes exhibit changes in the MH as manifested by a decline in streamflow, especially in summer. Such flow decreases ~~in annual streamflow. The largest reduction occurs in September in MH$_{GS}$, one month later than in MH$_{REF}$. These~~ are a combined effect of changes in ~~the simulated streamflow were determined to be the combined effects of changes in rainfall~~ snowmelt and evapotranspiration. ~~The~~A significant amount of solid precipitation shifts to liquid precipitation and the JJAS net precipitation is simulated to shrink ~~by about 30% in MH$_{REF}$ and 10% in MH$_{GS}$. Snowmelt also plays a modest role in UYEB hydrology.~~in both MH experiments. The GS forcing caused a rise in temperature during the MH, as well as larger rainfall but smaller snowmelt and lager evaporative water losses compared to the MH$_{REF}$.

~~The most important change in the MH in the UYAB is a significant shift from solid to liquid precipitation. Both MH experiments show a decrease in annual snowmelt (17% in MH$_{REF}$ and 19% in MH$_{GS}$, with ±10% variability between ensemble members); a warming of 1.3 °C is simulated in MH$_{GS}$ while a small annual cooling is shown in the WRF experiments without the GS boundary forcing. The standard MH experiments produce a 9% annual precipitation decrease, while MH$_{GS}$ shows a small increase of approximately 4%. However, the net effect of all these changes in both MH experiments is a large reduction in streamflow, especially in summer.~~

In the UBB, the simulated annual total precipitation increase in the MH is the largest among three basins~~: about 11% in the ensemble mean in MH$_{REF}$ and 26% in MH$_{GS}$. The simulated JJAS warming is 0.5 °C in MH$_{REF}$,~~ and ~~1.5 °C in MH$_{GS}$, but~~, unlike the ~~UYAB, the amount of solid precipitation changes little because the amount of snowfall in PI is much smaller than that in UYAB. Based on the simulations presented here~~other two basins, the most significant MH hydroclimatic anomaly ~~in~~over the UBB may be an ~~increased~~increase in runoff ~~(~27% in MH$_{REF}$ and ~55% in MH$_{GS}$), especially~~both MH experiments, particularly in mid-summer, ~~because of~~due to greater net precipitation ~~and runoff generation~~. The greening of the Sahara led to higher temperature and enhanced snowmelt in spring and eliminated the drop in runoff in April in MH$_{REF}$.

~~A~~ One of the most fundamental ~~uncertainty limiting~~uncertainties that limit the validity of the MH simulations ~~presented herein~~in this study is natural variability, including the El Niño–Southern Oscillation. This ~~clearly underscores the need~~calls for an initial condition ensemble where the RCM is forced with different periods of the global simulations. Besides, this study has used only one coupled regional modeling system to investigate the influence on the TP climate only due to the MH land cover changes over northern Africa. However, ~~some recent studies~~ reduced dust emissions from the Sahara during the MH

19

have also ~~argue for an impact on the MH~~ been suggested to play a role in modulating the Asian monsoon ~~resulting from reduced dust over northern Africa~~ (Sun et al., 2019; Pausata et al., 2020). ~~Additionally~~Moreover, reconstructions ~~indicate widespread vegetation~~suggest extensive land cover changes during the MH, ~~particularly greater~~in particular higher vegetation coverage ~~over Eurasia~~on the Eurasian continent (Tarasov et al., 1998; Zhang et al., 2014; Li et al., 2019; Chen et al., 2020b), which has been shown to ~~be able to shift~~have global influence by shifting the latitudinal position of the of the intertropical convergence zone ~~northward and have a global impact~~ (Swann et al., 2014). These ~~results call for~~all underscore the necessity of further studies ~~using both~~over the TP based on different ~~numerical~~climate models ~~and~~, as well as more realistic dust concentrations and ~~vegetation distributions~~land cover in the paleoclimate simulations ~~over the TP~~.

Appendix A
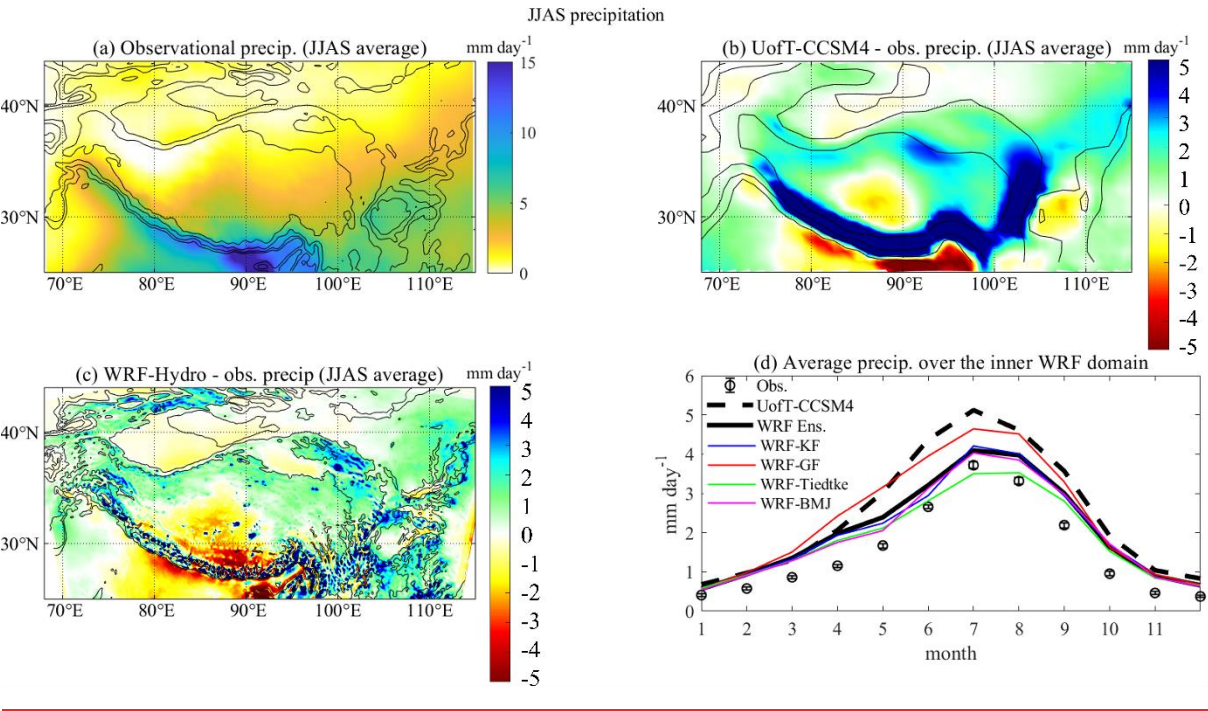
Figure A1: JJAS precipitation bias with respect to (a) the CRU observational dataset for (b) the UofT-CCSM4 and (c) the WRF ensemble. (c) Monthly precipitation over the inner WRF domain in the observation, UofT-CCSM4, WRF ensemble average and four individual physics ensemble members. The topography contours of 500, 1000, 2000, and 4000 m are also shown in black in (a, b, c).

Code/Data availability

Code and data for reproducing ~~each of~~ the figures in the ~~paper~~article can be obtained from Yiling Huo.

Author contribution

WRP and YH designed the experiments and YH ~~carried them out.~~constructed the simulations. DC designed the ~~Green Sahara~~GS simulation and performed the UofT-CCSM4 global experiments. ~~YH adapted the WRF radiation module for the MH experiments with the help of DC.~~ YH modified the dynamical downscaling pipeline to include WRF-Hydro. YH prepared the manuscript with contributions from both co-authors.

Competing interests

The authors declare that they have no conflict of interest.

Acknowledgments

The simulations ~~presented~~analyzed in this ~~paper~~study were performed ~~at~~on the Niagara supercomputer, which is operated by the SciNet High Performance Computing facility at the University of Toronto~~, which~~. SciNet is a component of the Compute Canada ~~HPC~~high-performance computing platform.

Financial support

This research has been ~~supported~~funded by the Natural Sciences and Engineering Research Council of Canada ~~(grant no.~~ A9627~~).~~ to WRP.

References

An, Z., Kutzbach, J., Prell, W., and Porter, S.: Evolution of Asian monsoons and phased uplift of the Himalaya–Tibetan plateau since Late Miocene times, Nature, 411, 62–66, https://doi.org/10.1038/35075035, 2001.

Barnett, T. P., Adam, J. C., and Lettenmaier, D. P.: Potential impacts of a warming climate on water availability in snow-dominated regions, Nature, 438, 303–309, https://doi.org/10.1038/nature04141, 2005.

Bartlein, P. J., Harrison, S. P., Brewer, S., Connor, S., Davis, B. A. S., Gajeweski, K., Guiot, J., Harrison-Prentice, T. I., Henderson, A., Peyron, O., Prentice, I. C., Scholze, M., Seppä, H., Shuman, B., Sugita, S., Thompson, R. S., Viau, A. E., Williams, J., and Wu, H.: Pollen-based continental climate reconstructions at 6 and 21 ka: a global synthesis, Clim. Dynam.,37, 775–802, https://doi.org/10.1007/s00382-010-0904-1, 2011.

Berger, A.: Long-term variations of daily insolation and quater-nary climatic changes, J. Atmos. Sci., 35, 2362–2367, https://doi.org/10.1175/1520-0469(1978)035<2362:LTVODI>2.0.CO;2, 1978.

Cai, M., Yang, S., Zhao, C., Zhou, Q., and Hou, L.: Insight into runoff characteristics using hydrological modeling in the data-scarce southern Tibetan Plateau: Past, present, and future, PLoS ONE, 12(5), e0176813. https://doi.org/10.1371/journal.pone.0176813, 2017.

Chandan, D. and Peltier, W. R.: Regional and global climate for the mid-Pliocene using the University of Toronto version of CCSM4 and PlioMIP2 boundary conditions, Clim. Past, 13, 919–942, https://doi.org/10.5194/cp-13-919-2017, 2017.

Chandan, D. and Peltier, W. R.: On the mechanisms of warming the mid-Pliocene and the inference of a hierarchy of climate sensitivities with relevance to the understanding of climate futures, Clim. Past, 14, 825–856, https://doi.org/10.5194/cp-14-825-2018, 2018.

Chandan, D. and Peltier, W. R.: African Humid Period precipitation sustained by robust vegetation, soil, and lake feedbacks, Geophys. Res. Lett., 47, e2020GL088728, https://doi.org/10.1029/2020GL088728, 2020.

Chen, X., Wu, D., Huang, X., Lv, F., Brenner, M., Jin, H., Chen, F.:Vegetation response in subtropical southwest China to rapid climate change during the Younger Dryas, Earth Sci. Rev., 201, p. 103080, https://doi.org/10.1016/j.earscirev.2020.103080, 2020a.

Chen, F., Zhang, J., Liu, J., Cao, X., Hou, J., Zhu, L., Xu, X., Liu, X., Wang, M., Wu, D., Huang, L., Zeng, T., Zhang, S., Huang, W., Zhang, X., and Yang, K.: Climate change, vegetation history, and landscape responses on the Tibetan Plateau during the Holocene: a comprehensive review, Quaternary Science Reviews, 243, 106444, https://doi.org/10.1016/j.quascirev.2020.106444, 2020b.

Conroy, J. L., and Overpeck, J. T.: Regionalization of Present-Day Precipitation in the Greater Monsoon Region of Asia, J. Clim., 24, 4073–4095. doi:10.1175/2011JCLI4033.1, 2011.

Cuo, L., Zhang, Y., Gao, Y., Hao, Z. and Cairang, L.: The impacts of climate change and land cover/use transition on the hydrology in the upper Yellow River Basin, China, Journal of Hydrology, 502, 37-52, https://doi.org/10.1016/j.jhydrol.2013.08.003, 2013.

d'Orgeville, M., Peltier, W. R., Erler, A. R., and Gula, J.: Climate change impacts on Great Lakes Basin precipitation extremes, J. Geophys. Res., 119, 10 799–10 812, https://doi.org/10.1002/2014JD021855, 2014.

Erler, A. R. and Peltier, W. R.: Projected Changes in Precipitation Extremes for Western Canada based on High-resolution Regional Climate Simulations, J. Climate, 29, 8841–8863, https://doi.org/10.1175/JCLI-D-15-0530.1, 2016.

Gent, P. R., Danabasoglu, G., Donner, L. J., Holland, M. M, Hunke, E. C., Jayne, S. R., Lawrence, D. M., Neale, R. B., Rasch, P. J., Vertenstein, M., Worley, P. H., Yang, Z.-L., and Zhang, M.: The community climate system model version 4, J. Climate, 24, 4973–4991, https://doi.org/10.1175/2011JCLI4083.1, 2011.

Gochis, D.J., Barlage, M., Cabell, R., Casali, M., Dugger, A., FitzGerald, K., McAllister, M., McCreight, J., RafieeiNasab, A., Read, L., Sampson, K., Yates, D., and Zhang, Y.: The WRF-Hydro modeling system technical description, (Version 5.1.1), NCAR Technical Note, available at: https://ral.ucar.edu/sites/default/files/public/WRFHydroV511TechnicalDescription.pdf, 2020.

Gochis, D. J., and Chen, F.: Hydrological Enhancements to the Community Noah Land Surface Model: Technical Description; Center for Atmospheric Research (NCAR): Boulder, CO, USA, 2003.

695 GRDC: Report of the Twelfth Meeting of the GRDC Steering Committee, Koblenz, Germany, 18–19 June 2014, Global Runoff Data Centre (GRDC), Koblenz, Germany, 23 pp, https://doi.org/10.5675/GRDC_Report_46, 2015.

Gula, J. and W. R. Peltier: Dynamical downscaling over the Great Lakes Basin of North America using the WRF regional climate model: The impact of the Great Lakes system on regional greenhouse warming, J. Climate, 25, 7723–7742, https://doi.org/10.1175/JCLI-D-11-00388.1, 2012.

Harris, I., Osborn, T.J., Jones, P., and Lister, D.: Version 4 of the CRU TS monthly high-resolution gridded multivariate

700 climate dataset, Sci Data 7, 109, https://doi.org/10.1038/s41597-020-0453-3, 2020.

Hély, C., Lézine, A. M., and Contributors, A. P. D.: Holocene changes in African vegetation: Tradeoff between climate and water availability, Climate of the Past, 10(2), 681–686, https://doi.org/10.5194/cp-10-681-2014, 2014.

Herzschuh, U.: Palaeo-moisture evolution in monsoonal Central Asia during the last 50.000 years, Quaternary Sci. Rev., 25 (1/2), 163-78, https://doi.org/10.1016/j.quascirev.2005.02.006, 2006.

705 Herzschuh, U., Cao, X., Laepple, T., Dallmeyer, A., Telford, R. J., Ni, J., Chen, F., Kong, Z., Liu, G., Liu, K., Liu, X., Stebich, M., Tang, L., Tian, F., Wang, Y., Wischnewski, J., Xu, Q., Yan, S., Yang, Z., Yu, G., Zhang, Y., Zhao, Y., and Zheng, Z.: Position and orientation of the westerly jet determined Holocene rainfall patterns in China, Nat. Commun., 10, 2376, https://doi.org/10.1038/s41467-019-09866-8, 2019.

Huang, Y., Cai, J., Yin, H., and Cai, M.: Correlation of precipitation to temperature variation in the Huanghe River (Yellow

710 River) basin during 1957–2006, Journal of Hydrology, 372, 1-8, https://doi.org/10.1016/j.jhydrol.2009.03.029, 2009.

Huo, Y. and Peltier, W. R.: Dynamically Downscaled Climate Simulations of the Indian Monsoon in the Instrumental Era: Physics Parameterization Impacts and Precipitation Extremes, J. Appl. Meteorol. Clim., 58, 831–852, https://doi.org/10.1175/JAMC-D18-0226.1, 2019.

Huo, Y. and Peltier, W. R.: Dynamically Downscaled Climate Change Projections for the South Asian Monsoon: Mean and

715 Extreme Precipitation Changes and Physics Parameterization Impacts, J. Climate, 33, 2311–2331, https://doi.org/10.1175/JCLID-19-0268.1, 2020.

Huo, Y. and Peltier, W. R.: The Southeast Asian Monsoon: Dynamically Downscaled Climate Change Projections and High Resolution Regional Ocean Modelling on the Effects of the Tibetan Plateau, Clim. Dynam., 56, 2597–2616, https://doi.org/10.1007/s00382-020-05604-9, 2021.

720 Huo, Y., Peltier, W. R., and Chandan, D.: Mid-Holocene monsoons in South and Southeast Asia: dynamically downscaled simulations and the influence of the Green Sahara, Clim. Past, 17, 1645–1664, https://doi.org/10.5194/cp-17-1645-2021, 2021.

Immerzeel, W. W., Lutz, A. F., Andrade, M., Bahl, A., Biemans, H., Bolch, T., Hyde, S., Brumby, S., Davies, B. J., Elmore, A. C., Emmer, A., Feng, M., Fernández, A., Haritashya, U., Kargel, J. S., Koppes, M., Kraaijenbrink, P. D. A., Kulkarni, A.

725 V., Mayewski, P. A., Nepal, S., Pacheco, P., Painter, T. H., Pellicciotti, Francesca, Rajaram, H., Rupper, S., Sinisalo, A.,

23

Shrestha, A. B., Viviroli, D., Wada, Y., Xiao, C., Yao, T. and Baillie, J. E. M.: Importance and vulnerability of the world's water towers, Nature, 577 (7790), 364-369, https://doi.org/10.1038/s41586-019-1822-y, 2020.

IPCC. Summary for Policymakers. In Climate Change 2013: The Physical Science Basis. Contribution of Working Group I to the Fifth Assessment Report of the Intergovernmental Panel on Climate Change, Cambridge University Press, Cambridge, United Kingdom and New York, NY, USA, 2013.

730

Kaser, G., Grosshauser, M., and Marzeion, B.: Contribution potential of glaciers to water availability in different climate regimes, Proc. Natl. Acad. Sci. USA, 107(47), 20,223–20,227, https://doi.org/10.1073/pnas.1008162107, 2010.

Kehrwald, N. M., Thompson, L. G., Tandong, Y., Mosley-Thompson, E., Schotterer, U., Alfimov, V., Beer, J., Eikenberg, J., and Davis, M. E.: Mass loss on Himalayan glacier endangers water resources, Geophys. Res. Lett., 35, L22503,

735   https://doi.org/10.1029/2008GL035556, 2008.

Kerandi, N., Arnault, J., Laux, P., Wagner, S., Kitheka, J., and Kunstmann, H.: Joint atmospheric-terrestrial water balances for East Africa: A WRF-Hydro case study for the upper Tana River basin, Theor. Appl. Climatol, 131, 1337–1355, https://doi.org/10.1007/s00704-017-2050-8, 2018.

Krysanova, V., Vetter, T., Eisner, S., Huang, S., Pechlivanidis, I., Strauch, M., Gelfan, A., Kumar, R., Aich, V., Arheimer,

740   B., Chamorro, A., van Griensven, A., Kundu, D., Lobanova, A., Mishra, V., Plötner, S., Reinhardt, J., Seidou, O., Wang, X., Wortmann, M., Zeng, X., and Hattermann, F. F.: Intercomparison of regional-scale hydrological models and climate change impacts projected for 12 large river basins worldwide—A synthesis, Environmental Research Letters, 12(10), 105002. https://doi.org/10.1088/1748-9326/aa8359, 2017.

Kaufman, D., McKay, N., Routson, C., et al.: A global database of Holocene paleotemperature records, Scientific data, 7(1),

745   1-34, https://doi.org/10.1038/s41597-020-0445-3, 2020.

Kutzbach, J. E., Prell, W. L., and Ruddiman, W. F.: Sensitivity of Eurasian climate to surface uplift of the Tibetan Plateau, J Geol, 101, 177–190, https://www.jstor.org/stable/30081146, 1993.

Lehnert, L., Wesche, K., Trachte, K., Reudenbach, C., and Bendix, J.: Climate variability rather than overstocking causes recent large scale cover changes of Tibetan pastures, Sci. Rep., 6, 24367, https://doi.org/10.1038/srep24367, 2016.

750   Li, Q., Wu, H., Yu, Y., Sun, A., and Luo, Y.: Large-scale vegetation history in China and its response to climate change since the Last Glacial Maximum, Quaternary International, 500, 108-119, https://doi.org/10.1016/j.quaint.2018.11.016, 2019.

Lu, H., Wu, N., Liu, K., Zhu, L., Yang, X., Yao, T., Wang, L., Li, Q., Liu, X., Shen, C., Li, X., Tong, G., and Jiang, H.: Modern pollen distributions in Qinghai-Tibetan Plateau and the development of transfer functions for reconstructing Holocene environmental changes, Quat. Sci. Rev., 30, 947–966, https://doi.org/10.1016/j.quascirev.2011.01.008, 2011.

755   Ma, Q., Zhu, L., Lü, X., Guo, Y., Ju, J., Wang, J., Wang, Y., and Tang, L.: Pollen-inferred Holocene vegetation and climate histories in Taro Co, southwestern Tibetan Plateau, Chin. Sci. Bull, 59, 4101–4114, https://doi.org/10.1007/s11434-014-0505-1, 2014.

Maher, B. A.: Holocene variability of the East Asian summer monsoon from Chinese cave records: a re-assessment, Holocene, 18, 861–866, https://doi.org/10.1177/0959683608095569, 2008.

Molnar, P., Boos, W. R., and Battisti, D. S.: Orographic controls on climate and paleoclimate of asia: thermal and mechanical roles for the Tibetan Plateau, Annu. Rev. Earth Planet. Sci, 38, 77–102, https://doi.org/10.1146/annurev-earth-040809-152456, 2010.

Otto-Bliesner, B. L., Braconnot, P., Harrison, S. P., Lunt, D. J., Abe-Ouchi, A., Albani, S., Bartlein, P. J., Capron, E., Carlson, A. E., Dutton, A., Fischer, H., Goelzer, H., Govin, A., Haywood, A., Joos, F., LeGrande, A. N., Lipscomb, W. H., Lohmann, G., Mahowald, N., Nehrbass-Ahles, C., Pausata, F. S. R., Peterschmitt, J.-Y., Phipps, S. J., Renssen, H., and Zhang, Q.: The PMIP4 contribution to CMIP6 – Part 2: Two interglacials, scientific objective and experimental design for Holocene and Last Interglacial simulations, Geosci. Model Dev., 10, 3979–4003, https://doi.org/10.5194/gmd-10-3979-2017, 2017.

Pausata, F. S. R., Gaetani, M., Messori, G., Berg, A., Maia de Souza, D., Sage, R. F., and deMenocal, P. B.: The Greening of the Sahara: Past Changes and Future Implications, One Earth, 2, 235–250, https://doi.org/10.1016/j.oneear.2020.03.002, 2020.

~~Peltier, W. R., d'Orgeville, M., Erler, A. R., and Xie, F.: Uncertainty in Future Summer Precipitation in the Laurentian Great Lakes Basin: Dynamical Downscaling and the Influence of Continental Scale Processes on Regional Climate Change, J. Climate, 31, 2651–2673, https://doi.org/10.1175/JCLI-D-17-0416.1, 2018.~~

Pausata, F. S. R., Messori, G., and Zhang, Q.: Impacts of dust reduction on the Northward expansion of the African monsoon during the Green Sahara period, Earth and Planetary Science Letters, 434, 298–307. https://doi.org/10.1016/j.epsl.2015.11.049, 2016.

Pausata, F., Zhang, Q., Muschitiello, F., Lu, Z., Chafik, L., Niedermeyer, E. M., Stager J. C., Cobb, K. M., and Liu, Z.: Greening of the Sahara suppressed ENSO activity during the mid-Holocene, Nat Commun, 8, 16020, https://doi.org/10.1038/ncomms16020, 2017.

Peltier, W. R., d'Orgeville, M., Erler, A. R., and Xie, F.: Uncertainty in Future Summer Precipitation in the Laurentian Great Lakes Basin: Dynamical Downscaling and the Influence of Continental Scale Processes on Regional Climate Change, J. Climate, 31, 2651–2673, https://doi.org/10.1175/JCLI-D-17-0416.1, 2018.

Peltier, W. R. and Vettoretti, G.: Dansgaard-Oeschger oscillations predicted in a comprehensive model of glacial climate: A "kicked" salt oscillator in the Atlantic, Geophys. Res. Lett., 41, 7306–7313, https://doi.org/10.1002/2014GL061413, 2014

Scussolini, P., Eilander, D., Sutanudjaja, E. H., Ikeuchi, H., Hoch, J. M., Ward, P. J., Bakker, P., Otto-Bliesner, B. L., Guo, C., Stepanek, C., Zhang, Q., Braconnot, P., Guarino, M.-V., Muis, S., Yamazaki, D., Veldkamp, T. I. E., and Aerts, J. C. J. H.: Global river discharge and floods in the warmer climate of the Last Interglacial, Geophys. Res. Lett., 47, e2020GL089375, https://doi.org/10.1029/2020GL089375, 2020.

Senatore, A., Mendicino, G., Gochis, D. J., Yu, W., Yates, D. N., and Kunstmann, H.: Fully coupled atmosphere-hydrology simulations for the central Mediterranean: Impact of enhanced hydrological parameterization for short and long time scales, J. Adv. Model. Earth Syst.,7, 1693–1715, https://doi.org/10.1002/2015MS000510, 2015.

Shi, Y. F., Kong, Z. Z., Wang, S. M., Tang, L. Y., Wang, F. B., Yao, T. D., Zhao, X. T., Zhang, P. Y., and Shi, S. H.: Mid-Holocene climates and environments in China, Global Planet. Change, 7, 219–233, https://doi.org/10.1016/0921-8181(93)90052-P, 1993.

Shi, P. J. and Song, C. Q.: Palynological records of environmental changes in the middle part of Inner Mongolia, China, Chin. Sci. Bull., 48, 1433–1438, https://doi.org/10.1360/02wd0259, 2003.

Skinner, C. B. and Poulsen, C. J.: The role of fall season tropical plumes in enhancing Saharan rainfall during the African Humid Period, Geophysical Research Letters, 43 (1), 349–358, https://doi.org/10.1002/2015GL066318, 2016.

Somos-Valenzuela, M. A. and Palmer, R. N.: Use of WRF-Hydro over the Northeast of the US to Estimate Water Budget Tendencies in Small Watersheds, Water, 10, 1709, https://doi.org/10.3390/w10121709, 2018.

Sun, W., Wang, B., Zhang, Q., Pausata, F. S. R., Chen, D., Lu, G., Yan, M., Ning, L., and Liu, J.: Northern Hemisphere Land Monsoon Precipitation Increased by the Green Sahara During Middle Holocene, Geophys. Res. Lett., 46, 9870–9879, https://doi.org/10.1029/2019GL082116, 2019.

Sun, Q. L., Zhou, J., Shen, J., Chen, P., Wu, F., and Xie, X. P.: Environmental characteristics of Mid-Holocene recorded by lacustrine sediments from Lake Daihai, north environment sensitive zone, China, Sci. China Ser. D, 49, 968–981, https://doi.org/10.1007/s11430-006-0968-2, 2006.

Swann, A. L. S., Fung, I. Y., Liu, Y., and Chiang, J. C. H.: Remote Vegetation Feedbacks and the Mid-Holocene Green Sahara, J. Climate, 27, 4857–4870, https://doi.org/10.1175/JCLI-D-13-00690.1, 2014.

Tarasov, P. E., Webb III, T., Andreev, A. A., Afanas'eva, N. B., Berezina, N. A., Bezusko, L. G., Blyakharchuk, T. A., Bolikhovskaya, N. S., Cheddadi, R., Chernavskaya, M. M., Chernova, G. M., Dorofeyuk, N. I., Dirksen, V. G., Elina, G. A., Filimonova, L. V., Glebov, F. Z., Guiot, J., Gunova, V. S., Harrison, S. P., Jolly, D., Khomutova, V. I., Kvavadze, E. V., Osipova, I. M., Panova, N. K., Prentice, I. C., Saarse, L., Sevastyanov, D. V., Volkova, V. S., and Zernitskaya, V. P.: Presentday and mid-Holocene biomes reconstructed from pollen and plant macrofossil data from the former Soviet Union and Mongolia, J. Biogeogr., 25, 1029–1053, https://doi.org/10.1046/j.1365-2699.1998.00236.x, 1998.

Trambauer, P., Werner, M., Winsemius, H.C., Maskey, S., Dutra, E., and Uhlenbrook, S.: Hydrological drought forecasting and skill assessment for the Limpopo River basin, southern Africa, Hydrol. Earth Syst. Sci., 19, 1695–1711, https://doi.org/10.5194/hess-19-1695-2015, 2015.

Wang, M., Hou, J., Duan, Y., Chen, J., Li, X., He, Y., Lee, S. Chen, F.: Internal feedbacks forced Middle Holocene cooling on the Qinghai-Tibetan Plateau, Boreas, 50, 1116-1130, https://doi.org/10.1111/bor.12531, 2021.

Wanner, H., Beer, J., Bütikofer, J., Crowley, J. T., Cubasch, U., Flückiger, J., Goosse, H., Grosjean, M., Joos, F., Kaplan, J. O., Küttel, M., Müllerg, S. A., Prentice, I. C., Solomina, O., Stocker, T. F., Tarasov, P., Wagner, M., and Widmann, M.: Mid- to Late-Holocene climate change: An overview, Quaternary Science Reviews, 27, 1791–1828, https://doi.org/10.1016/j.quascirev.2008.06.013, 2008.

825 Yang, K., Wu, H., Qin, J., Lin, C., Tang, W., and Chen, Y.: Recent climate changes over the Tibetan Plateau and their impacts on energy and water cycle: A review, Glob. Planet Change, 112, 79-91, https://doi.org/10.1016/j.gloplacha.2013.12.001, 2014.

Yao, T., Thompson, L., Wei, Y., Yu, W., Yang, G., Guo, X., Yang, X., Duan, K., Zhao, H., and Xu, B.: Different glacier status with atmospheric circulations in Tibetan Plateau and surroundings, Nat. Clim. Change, 2, 663-667, 830 https://doi.org/10.1038/nclimate1580, 2012.

Yao, T., Xue, Y., Chen, D., Chen, F., Thompson, L., Cui, P., Koike, T., Lau, W. K.-M., Lettenmaier, D., and Mosbrugger, V.: Recent Third Pole's Rapid Warming Accompanies Cryospheric Melt and Water Cycle Intensification and Interactions between Monsoon and Environment: Multidisciplinary Approach with Observations, Modeling, and Analysis, Bull. Am. Meteorol. Soc., 100, 423-444, https://doi.org/10.1175/BAMS-D-17-0057.1, 2019.

835 Yao, T., Wang, Y., Liu, S., Pu, J., Shen, Y., and Lu, A.: Recent glacial retreat in High Asia in China and its impact on water resource in Northwest China, Sci. China, Ser. D Earth Sci., 47(12), 1065–1075, https://doi.org/10.1360/03yd0256, 2004.

Yao, T., and Yao, Z.: Impacts of glacier retreat on runoff on Tibetan Plateau (In Chinese), Chin. J. Nature, 32(1), 4–8, 2010.

Yatagai, A., Kamiguchi, K., Arakawa, O., Hamada, A., Yasutomi, N., and Kitoh A. APHRODITE: Constructing a Long-term Daily Gridded Precipitation Dataset for Asia based on a Dense Network of Rain Gauges, Bulletin of American 840 Meteorological Society, https://doi.org/10.1175/BAMS-D-11-00122.1, 2012.

Zhang, W., Ming, Q., Shi, Z., Chen, G., Niu, J., Lei, G., Chang, F., and Zhang, H.: Lake Sediment Records on Climate Change and Human Activities in the Xingyun Lake Catchment, SW China, PLoS One, 9, e102167, https://doi.org/10.1371/journal.pone.0102167, 2014.

Zhang, C., Zhao, C., Yu, S. Y., Yang, X., Cheng, J., Zhang, X., Xue, B., Shen, J., and Chen, F.: Seasonal imprint of 845 Holocene temperature reconstruction on the Tibetan Plateau. Earth-Science Reviews, 103927, https://doi.org/10.1016/j.earscirev.2022.103927, 2022.

Zheng, W., Wu, B., He, J., and Yu, Y.: The East Asian Summer Monsoon at mid-Holocene: results from PMIP3 simulations, Clim. Past, 9, 453–466, https://doi.org/10.5194/cp-9-453-2013, 2013.

Zhou, C. Y., Zhao, P., and Chen, J. M.: The interdecadal change of summer water vapor over the Tibetan Plateau and 850 associated mechanisms, J. Climate, 32, 4103–4119, https://doi.org/10.1175/JCLI-D-18-0364.1, 2019.
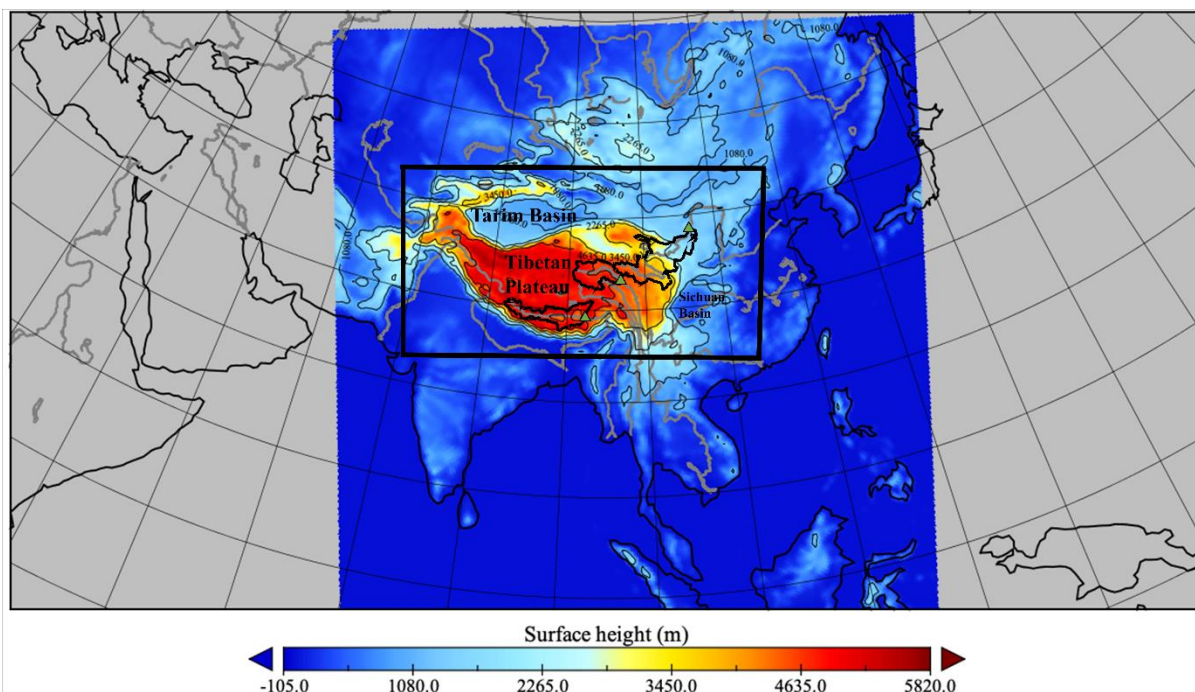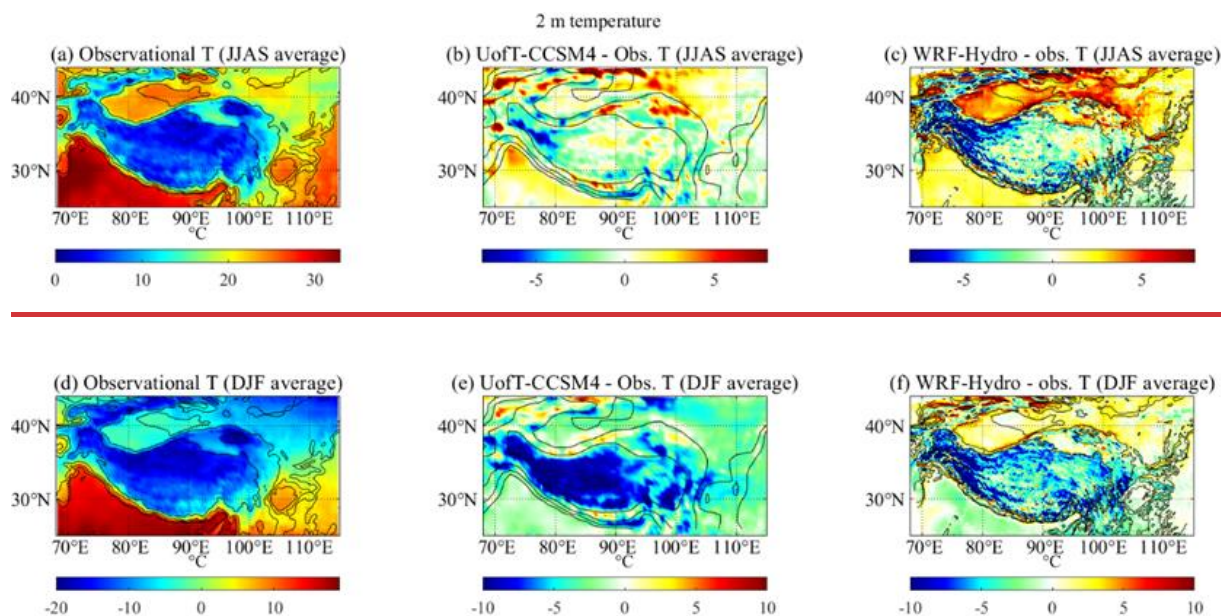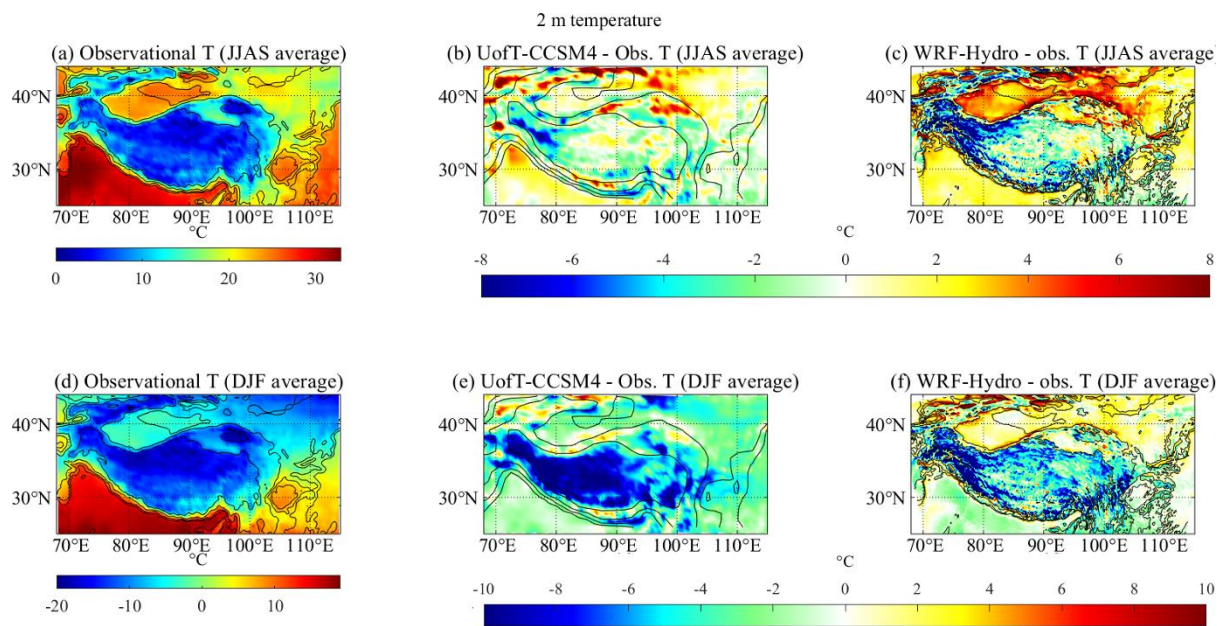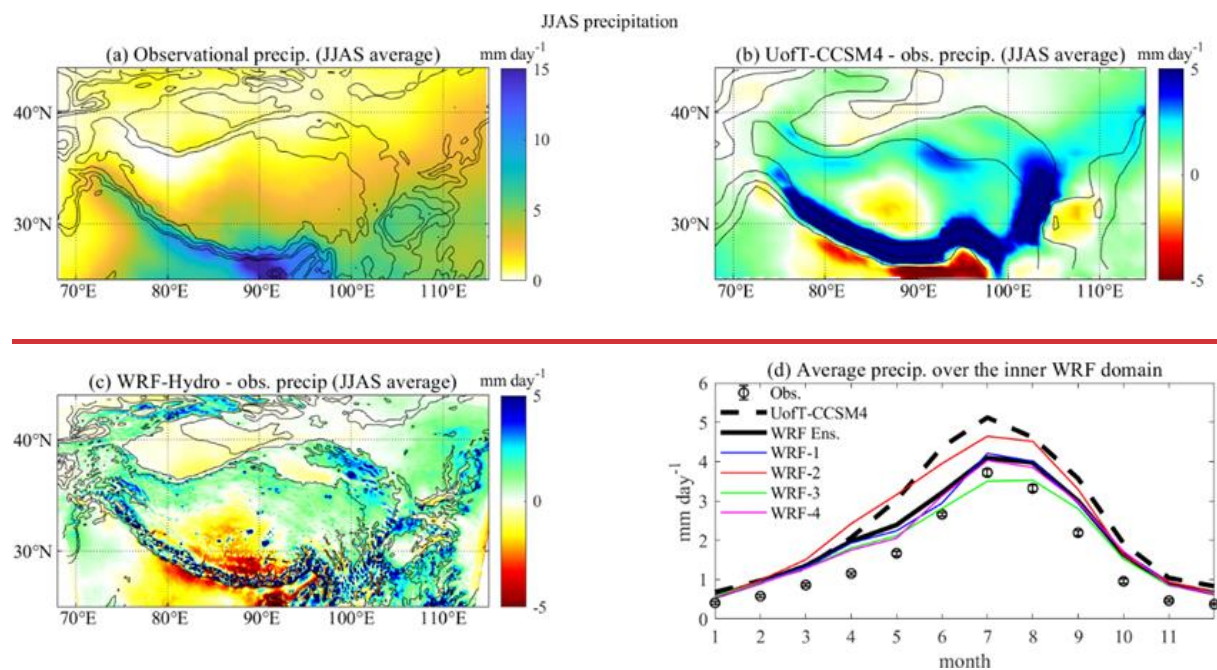
Figure 1: Topography (m) ~~and outlines of~~in **the outer** ~~and inner~~ **WRF** ~~domains~~domain, **as well as the major rivers and lakes (grey).**
The black rectangle represents the inner WRF domain. **Black curves denote outlines of the UBB, UYAB and UYEB at the left,**
middle and right. Green triangles inside each basin denote the Yangcun (left), Zhimenda (middle) and Tanglai Qu (right) stations.

28

2 m temperature

(a) Observational T (JJAS average)

(b) UofT-CCSM4 - Obs. T (JJAS average)

(c) WRF-Hydro - obs. T (JJAS average)

(d) Observational T (DJF average)

(e) UofT-CCSM4 - Obs. T (DJF average)

(f) WRF-Hydro - obs. T (DJF average)

Figure 2: Absolute 2-m air temperature bias with respect to (a, d) the CRU observational dataset for (b, e) the UofT-CCSM4 and (c, f) the WRF ensemble in (a, b, c) JJAS and (d, e, f) DJF. The topography contours of 500, 1000, 2000, and 4000 m are also shown in black.

JJAS precipitation

(a) Observational precip. (JJAS average)   mm day⁻¹

(b) UofT-CCSM4 - obs. precip. (JJAS average)   mm day⁻¹

(c) WRF-Hydro - obs. precip (JJAS average)   mm day⁻¹

(d) Average precip. over the inner WRF domain
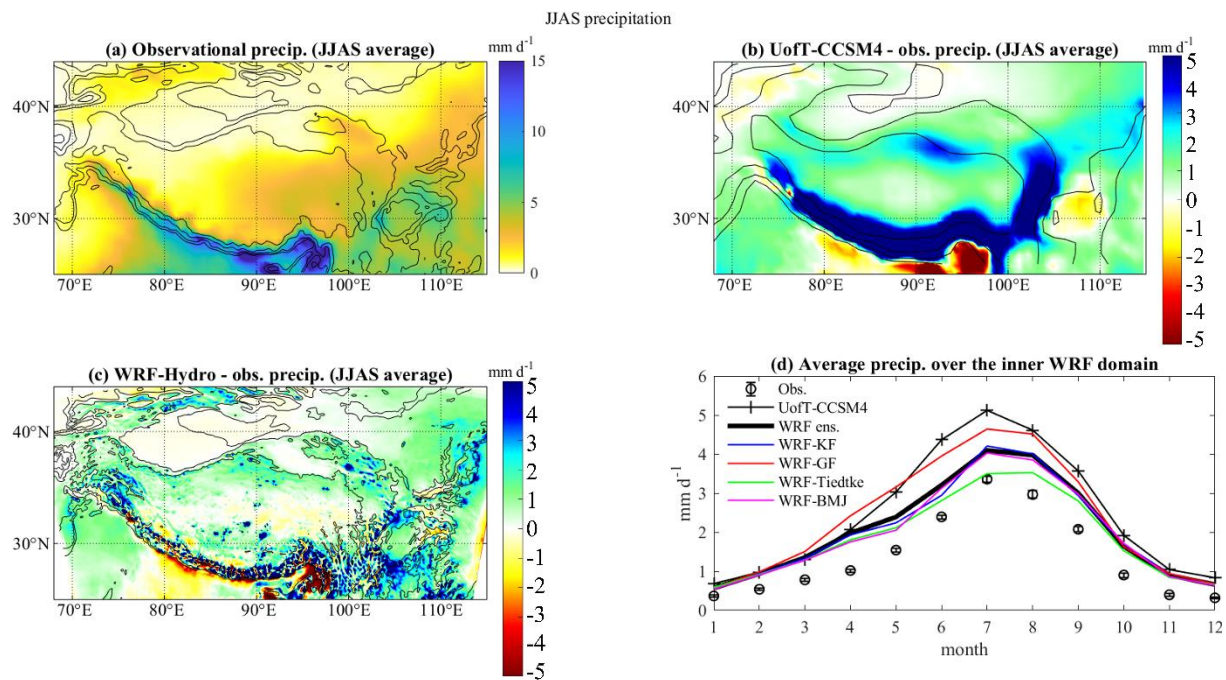
Figure 3: JJAS precipitation bias with respect to (a) the ~~CRU~~ APHRODITE observational dataset for (b) the UofT-CCSM4 and (c) the WRF ensemble. (c) Monthly precipitation over the inner WRF domain in the observation, UofT-CCSM4, WRF ensemble average and four individual physics ensemble members. The topography contours of 500, 1000, 2000, and 4000 m are also shown in black in (a, b, c).
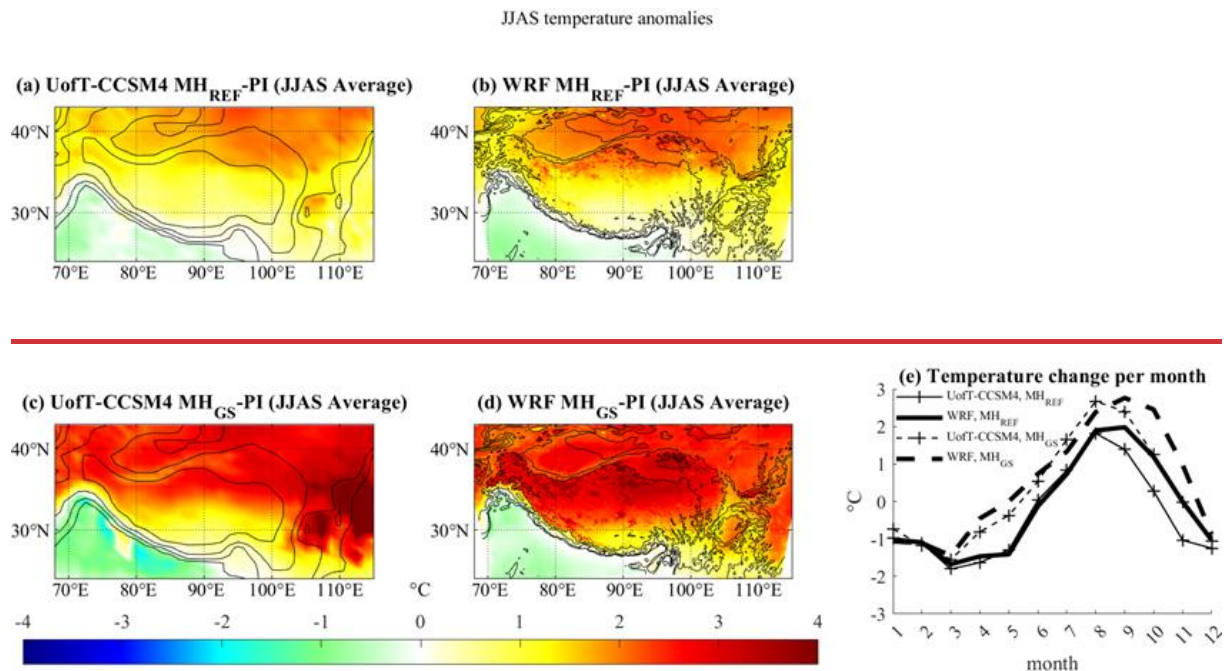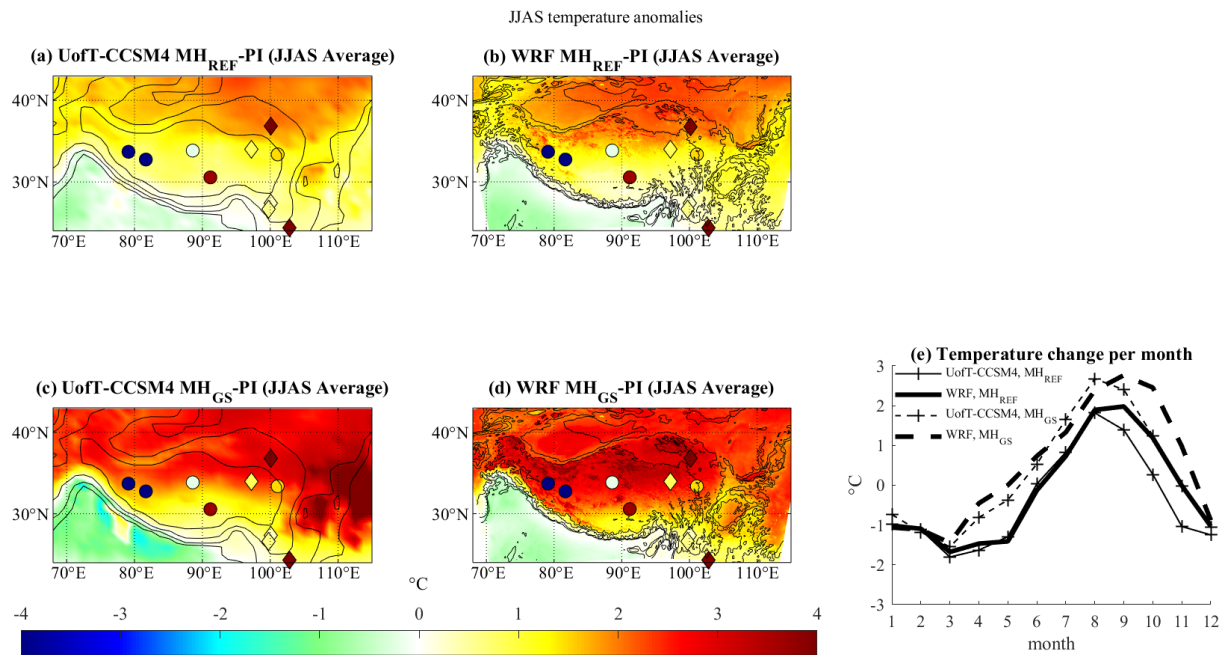
Figure 4: JJAS surface air temperature anomalies (°C) for (a, b) MH_{REF} and (c, d) MH_{GS} in (a, c) UofT-CCSM4 and the (b, d) WRF ensemble mean. (e) Monthly continental air temperature anomalies for MH_{REF} (solid) and MH_{GS} (dashed). ~~Shifts in calendar~~Reconstructed temperature differences between the MH and present day from Zhang et al. (2022) and Kaufman et al. (2020) are ~~not accounted for; i.e., the model calendar is used for the calculation of all anomalies.~~plotted as circles and diamonds, respectively. The topography contours (black) of 500, 1000, 2000, and 4000 m are ~~also~~ shown in (a-d).
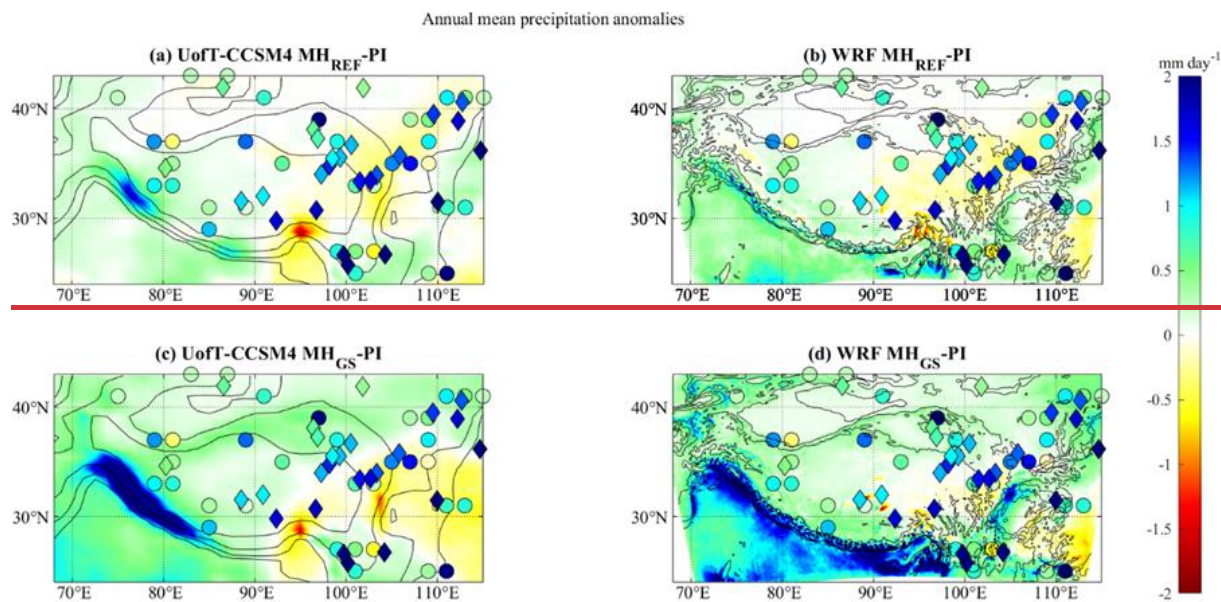
Figure 5: Annual mean precipitation anomalies (mm d⁻¹) for (a, b) MH_REF and (c, d) MH_GS in (a, c) UofT-CCSM4 and the (b, d) WRF ensemble mean. Reconstructed precipitation differences between the MH and present day from Bartlein et al. (2011) and Herzschuh et al. (2019) are plotted as circles and diamonds, respectively. The topography contours of 500, 1000, 2000, and 4000 m are also shown.
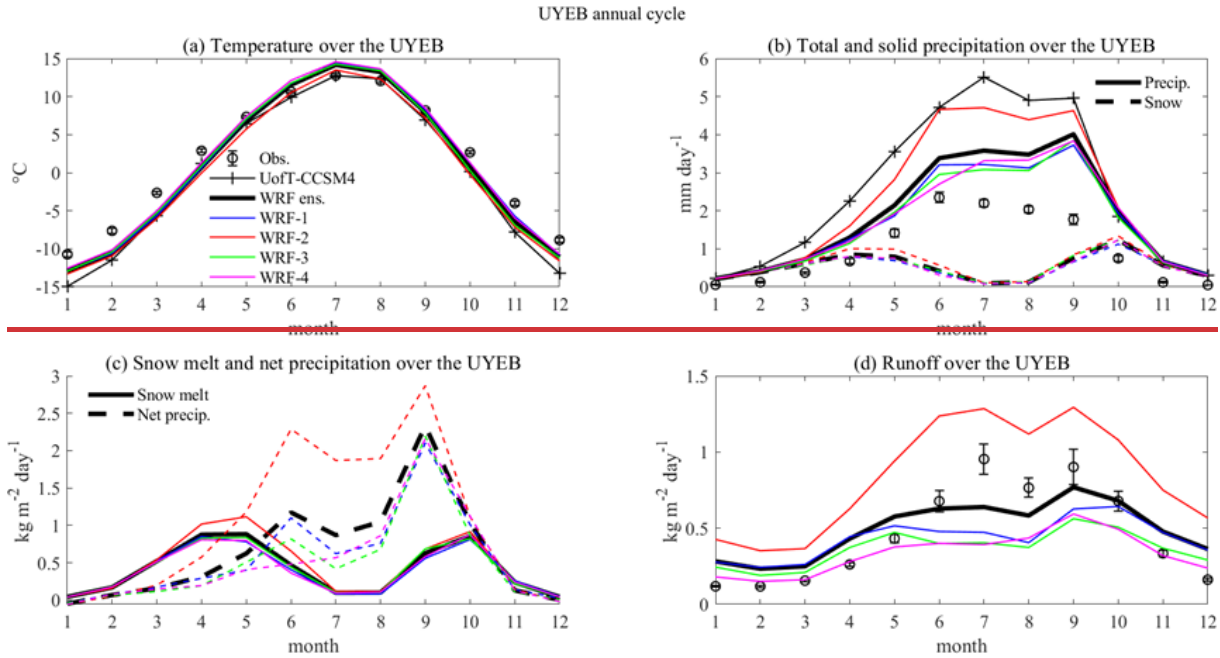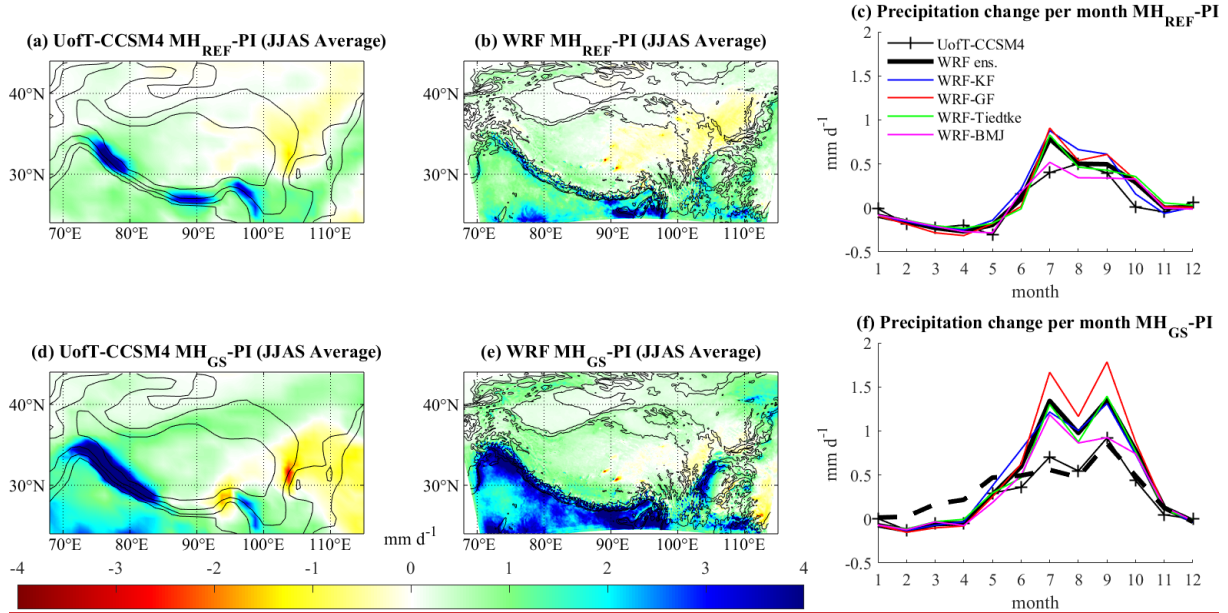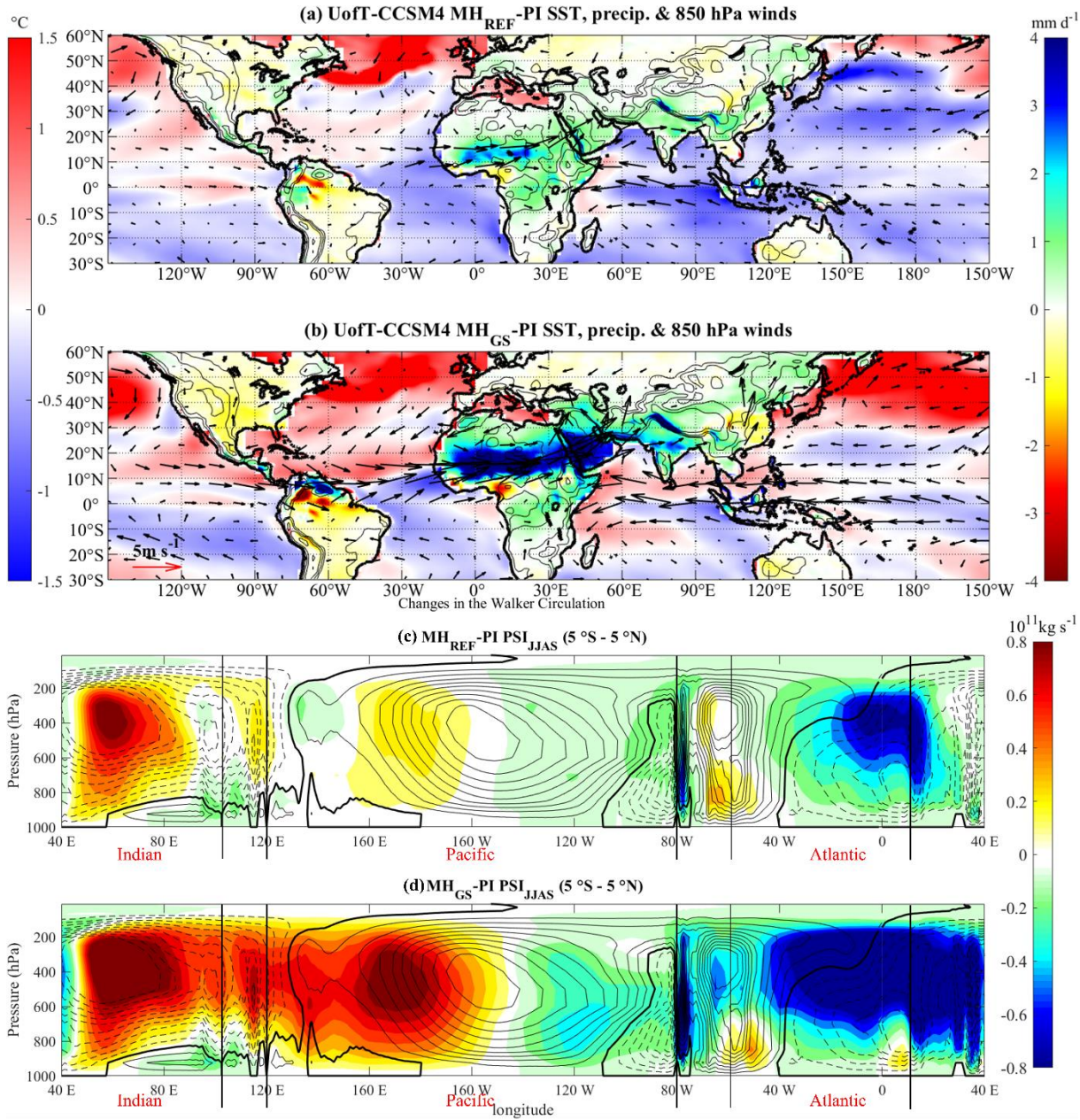
880

Figure 6: JJAS precipitation anomalies (mm d^{-1}) for (a, b) MH$_{REF}$ and (d, e) MH$_{GS}$ in (a, d) UofT-CCSM4 and the (b, e) WRF ensemble mean. Monthly precipitation anomalies (mm d^{-1}) in UofT-CCSM4 and four physics ensemble members over for (c) MH$_{REF}$ and (d) MH$_{GS}$. ~~Shifts in calendar are not accounted for; i.e., the model calendar is used for the calculation of all anomalies.~~ The dashed line in (f) represent the MH$_{GS}$–MH$_{REF}$ anomalies in the WRF ensemble mean. The topography contours of 500, 1000, 2000, and 4000 m are also shown in (a, b, d, e).

(a) UofT-CCSM4 MH$_{REF}$-PI SST, precip. & 850 hPa winds

(b) UofT-CCSM4 MH$_{GS}$-PI SST, precip. & 850 hPa winds

Changes in the Walker Circulation

(c) MH$_{REF}$-PI PSI$_{JJAS}$ (5 °S - 5 °N)

(d) MH$_{GS}$-PI PSI$_{JJAS}$ (5 °S - 5 °N)

890

Figure 7: SST (shaded, ° C), precipitation (shaded, mm d^{-1}) and 850 hPa winds (vector, m s^{-1}) anomalies during JJAS from the UofT-CCSM4 for (a) MH$_{REF}$ and (b) MH$_{GS}$. The topography contours of 500 m, 1000 m, 2000 m and 4000 m are also shown. PI climatological zonal stream function of the Walker circulation (contours: 0.2×10^{11} kg s^{-1} interval from -2 to 2×10^{11} kg s^{-1}; 0 line in bold) and associated changes (shaded) in (c) MH$_{REF}$ and (d) MH$_{GS}$ relative to the PI.

34
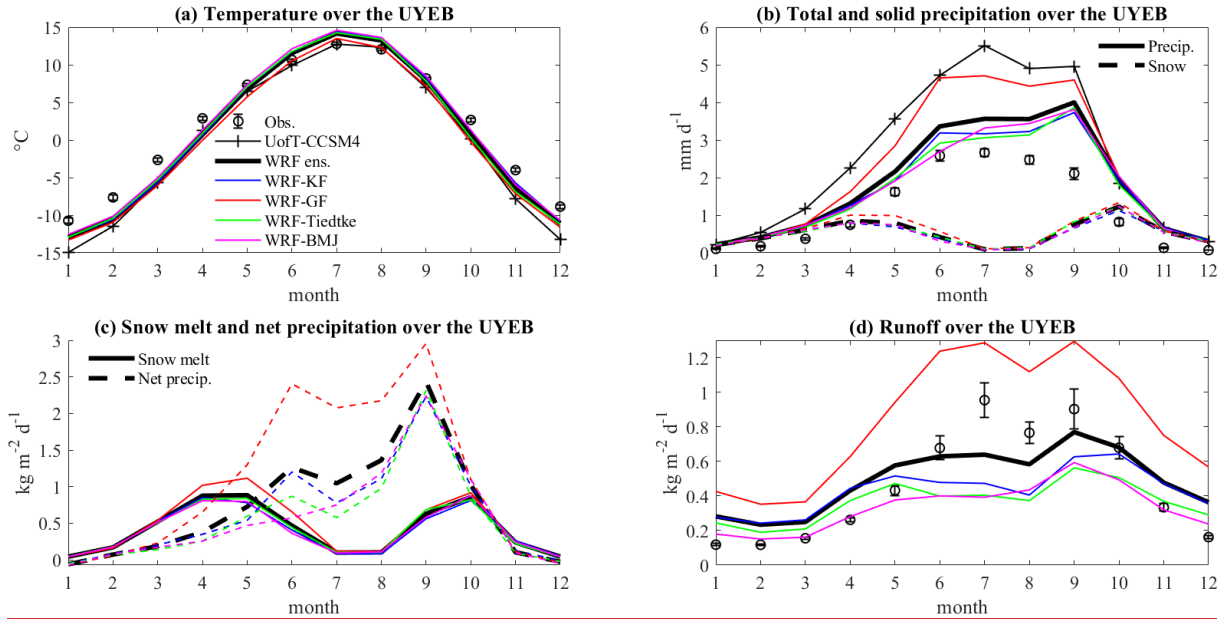
Figure 8: Average seasonal cycle over the UYEB: (a) temperature; (b) total and solid precipitation; (c) net precipitation and snowmelt and (d) discharge at the hydrometric station and total runoff from WRF. ~~All quantities are averaged over the entire basin; river discharge was normalized by the basin area.~~ The WRF ensemble average is shown in thick black lines, four individual ensemble members are shown by blue, red, green and magenta lines, respectively; ~~observed values~~observations are ~~indicated with~~represented by open circles. Error bars~~/bands~~ in (a, b, d) show the standard error of the mean ~~at a 95% confidence level~~.

UYAB annual cycle

(a) Temperature over the UYAB

(b) Total and solid precipitation over the UYAB

(c) Snow melt and net precipitation over the UYAB

(d) Runoff over the UYAB
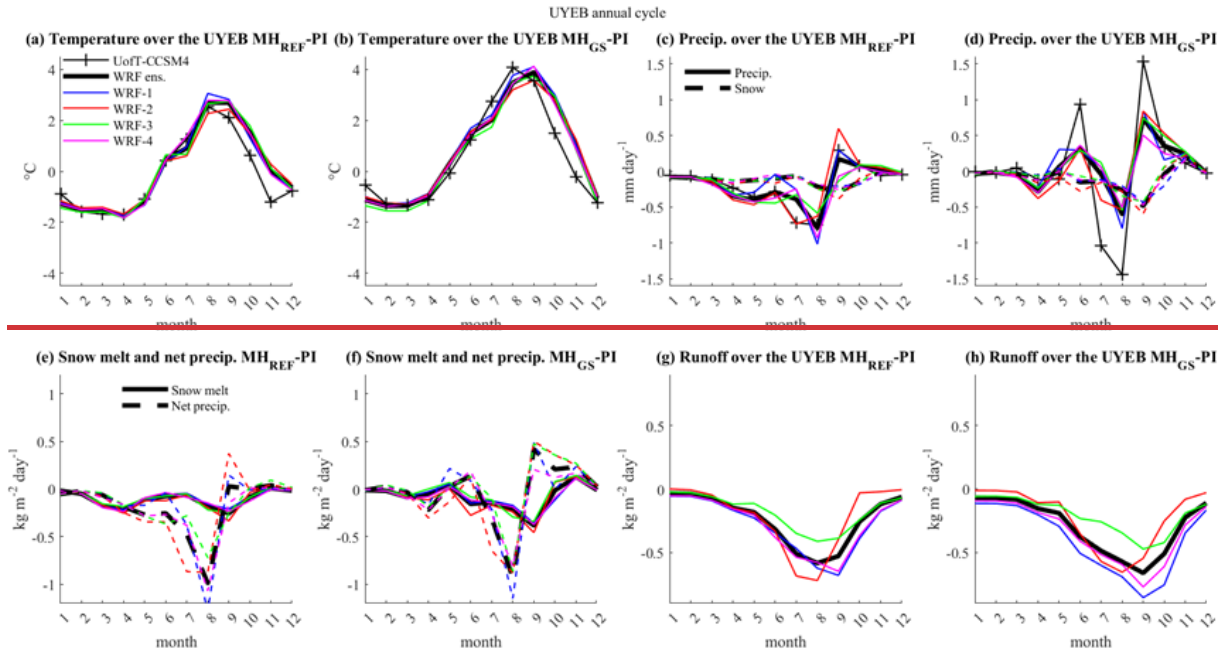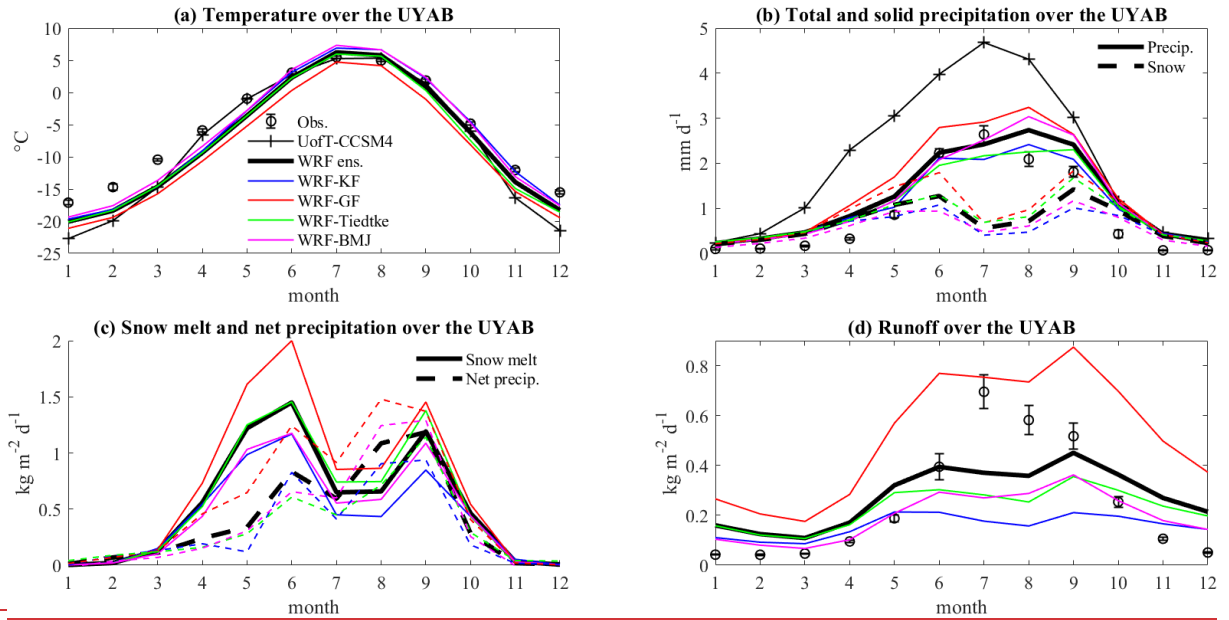
~~Figure 8:~~

Figure 9: As in Fig. 8, but for the UYAB.

UBB annual cycle

(a) Temperature over the UBB

(b) Total and solid precipitation over the UBB

(c) Snow melt and net precipitation over the UBB

(d) Runoff over the UBB
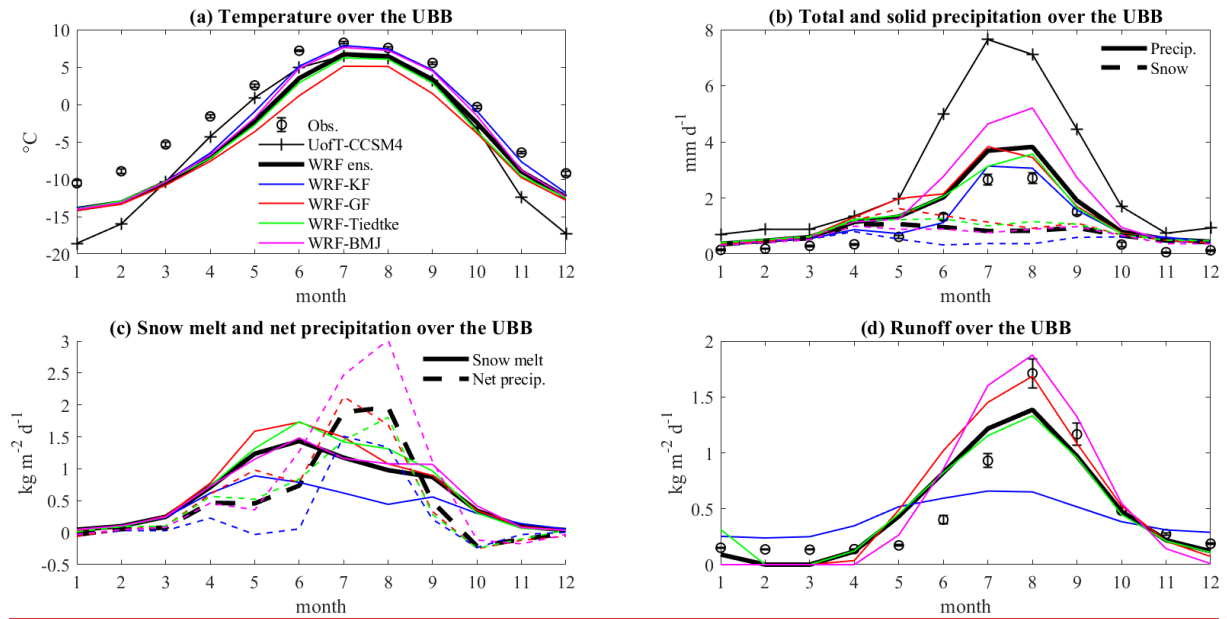
905   Figure 10: As in Fig. 8, but for the UBB.

Figure 11: Monthly anomalies ~~over the UYEB for~~of (a, ~~c, e, g) MH~~REF~~ and (b, d, f, h) MH~~GS of: (a, b) 2-m air) **temperature**~~; (e,~~ and (d-f) total and solid **precipitation**~~; (e, f~~ over the three basins.

Snow melt and net precipitation anomalies over the three river basins

(a) UYEB

(b) UYAB

(c) UBB

Runoff anomalies over the three river basins

(d) UYEB

(e) UYAB

(f) UBB
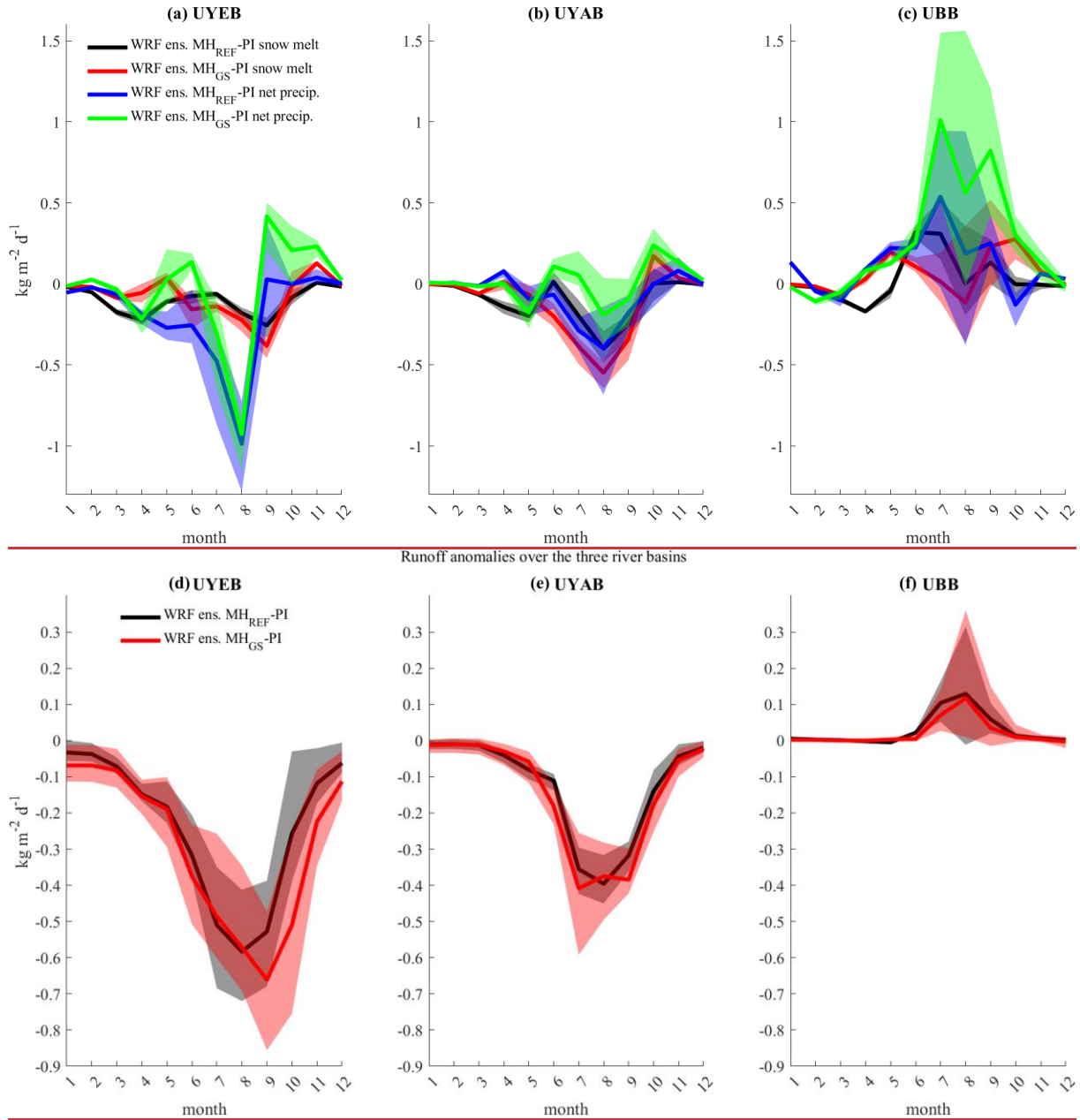
Figure 12: Monthly anomalies of (a-c) net precipitation and snowmelt and (g, h) riverd-f) total runoff. All quantities are averaged from WRF over the entire basin.

910
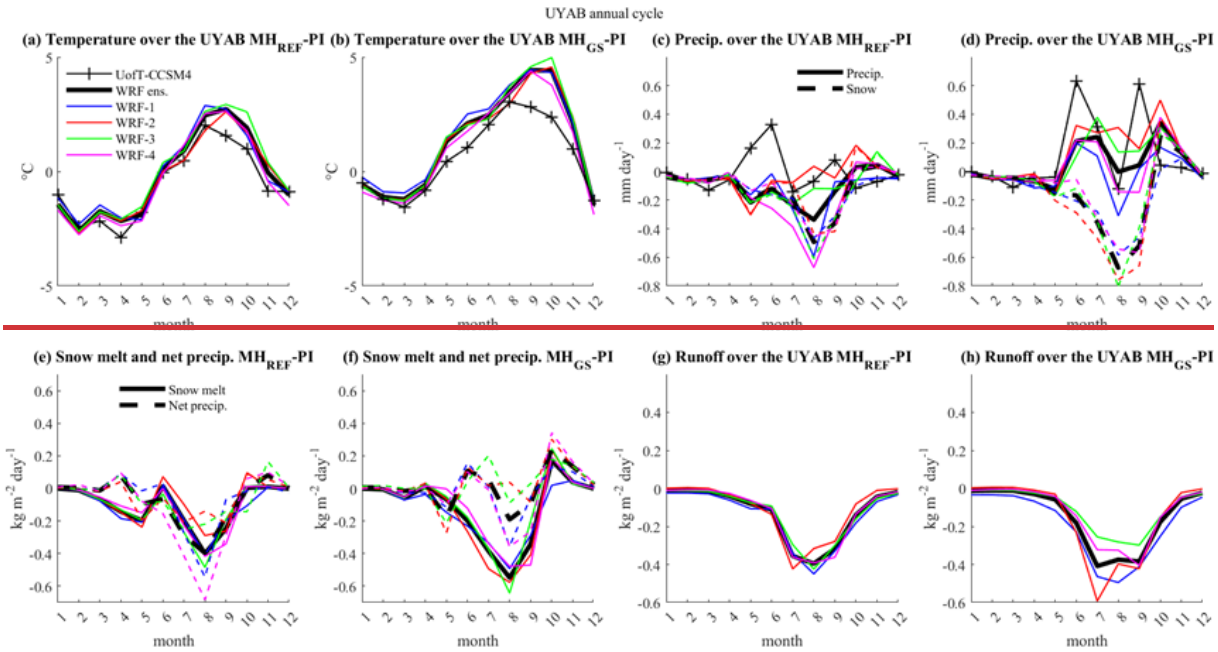
38
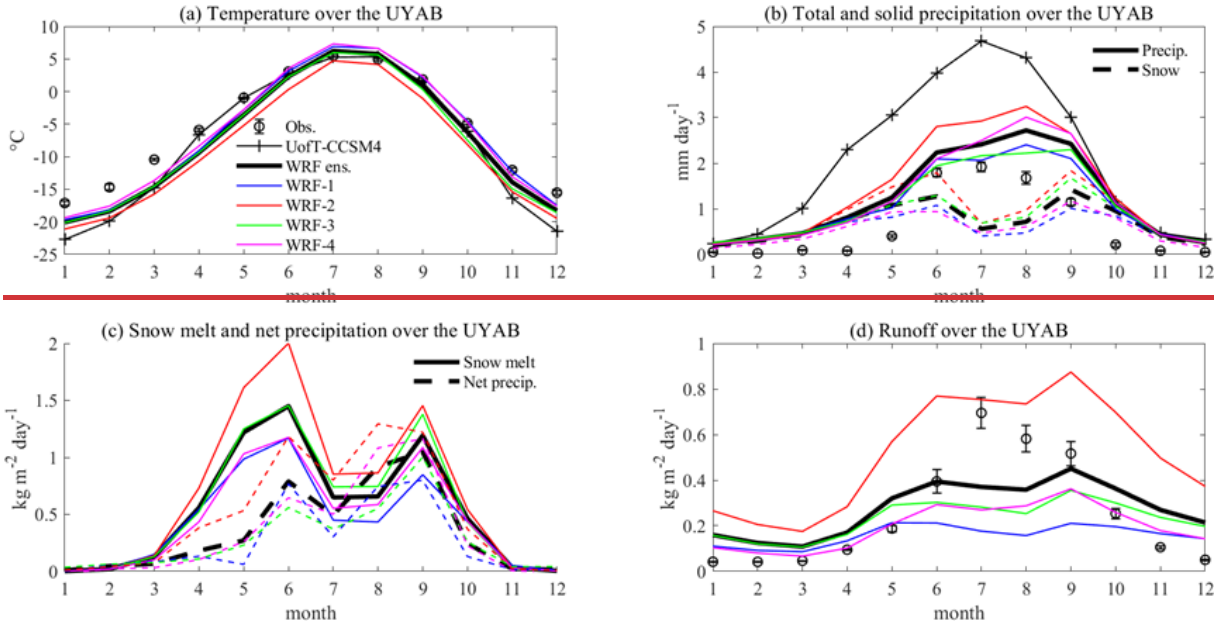
three basins Figure 9: As in Fig. 7, but for the UYAB.

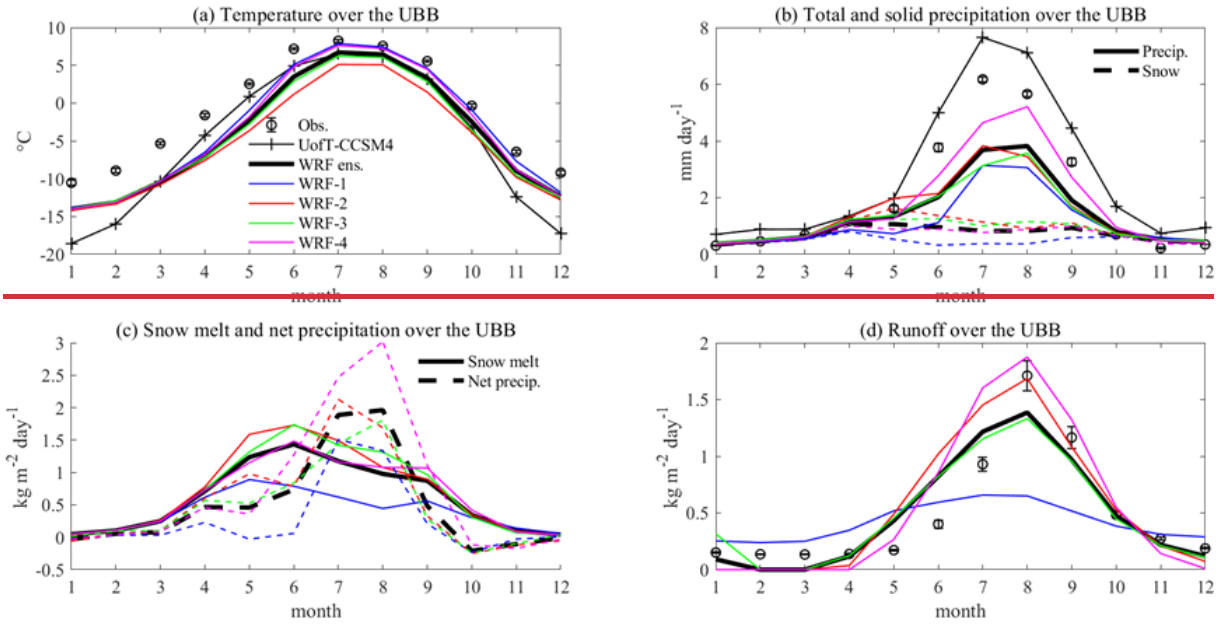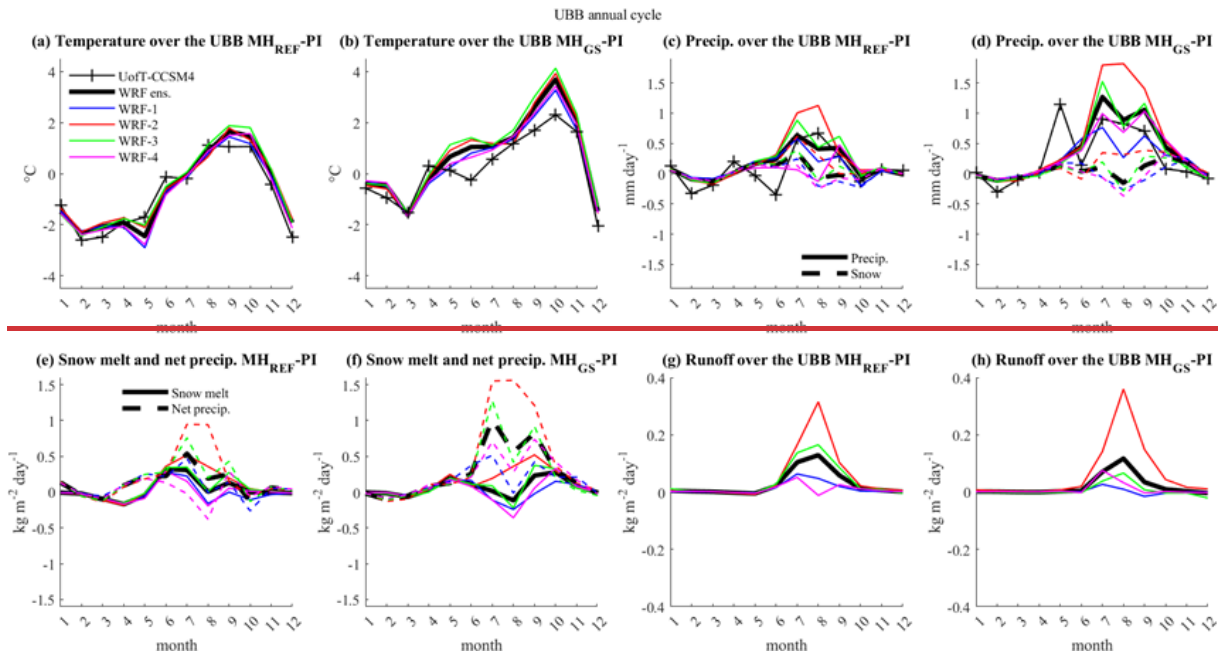Figure 10: As in Fig. 8, but for the UYAB.

Figure 11: As in Fig. 7, but for the UBB.

Figure 12: As in Fig. 8, but for the UBB.

920